

The Pennsylvania State University

The Graduate School

College of Engineering

**A SCALABLE HYBRID POWER AND ENERGY ARCHITECTURE  
FOR UNMANNED GROUND VEHICLES**

A Thesis in

Electrical Engineering

by

Nathaniel J. Hobbs

© 2010 Nathaniel J. Hobbs

Submitted in Partial Fulfillment  
of the Requirements  
for the Degree of

Master of Science

May 2010

The thesis of Nathaniel J. Hobbs was reviewed and approved\* by the following:

Heath Hofmann  
Adjunct Professor of Electrical Engineering, The Pennsylvania State University  
Associate Professor of Electrical Engineering, The University of Michigan  
Thesis Advisor

Jeffrey Mayer  
Associate Professor of Electrical Engineering

Karl Reichard  
Assistant Professor of Acoustics  
Research Associate, Applied Research Laboratory

Christopher Rogan  
Research Engineer, Applied Research Laboratory

Kenneth Jenkins  
Professor of Electrical Engineering  
Head of the Department of Electrical Engineering

\*Signatures are on file in the Graduate School

## **ABSTRACT**

Currently, the limiting factor in electric vehicle design and performance is the energy source. This problem has been recognized in the automotive industry, and much research has gone into alternatives to batteries, or augmenting them through a hybridization scheme. Very little of this research has gone into doing the same for robots. The research in the robotics field has focused mainly on integrating highly energy dense power sources with little thought applied to optimizing the efficiency of power converter designs and efficient energy management. There has been no effort to standardize the design of robot power systems through the use of a scalable power delivery architecture. The challenge lies in the development of the hardware and control algorithms for a scalable power delivery architecture which satisfies both the power and energy requirements of most unmanned ground vehicles. This thesis proposes a robotic power architecture which is easily scalable and facilitates the use of a wide variety of energy storage/generation devices, while focusing on the system control algorithm and its stability. The experimental results for an example system are presented, demonstrating that the architecture functions properly when faced with real world robotic power demands.

## TABLE OF CONTENTS

LIST OF FIGURES .....	vi
LIST OF TABLES .....	x
ACKNOWLEDGEMENTS .....	xi
Chapter 1 Hybrid Power and Energy for Robots (HyPER) .....	1
Currently Fielded Platforms and Uses .....	1
Hybrid Power and Energy Architecture Benefits .....	2
Proposed Hybrid Power and Energy Architecture .....	3
Summary .....	4
Chapter 2 Hardware Development .....	6
System Requirements .....	6
Energy Source Parameters .....	8
Bidirectional Converter Topology .....	8
Converter Component Design .....	10
Control Circuit .....	12
Complete Circuit .....	13
Converter Efficiency .....	14
Summary .....	16
Chapter 3 Supervisory Controller Development .....	18
High-level Controller Requirements .....	19
Low-level Controller Requirements .....	20
Summary .....	26
Chapter 4 HyPER System Simulation .....	27
System Model .....	27
Lumped Battery/Generator Model .....	29
Capacitor Model .....	29
Converter Model .....	30
Simulation Results .....	30
Summary .....	37
Chapter 5 Supervisory Controller Stability Analysis .....	38
Candidate Analysis Methods .....	39
System Model Assumptions .....	40
System Model Simplification .....	42
Mathematical Model .....	45

Model Simulation.....	49
Summary .....	56
Chapter 6 Converter Testing.....	57
Test Setup.....	57
Testing Results.....	58
Summary .....	65
Chapter 7 HyPER System Testing.....	66
HyPER Test Platform.....	66
Testing.....	70
Summary .....	75
Chapter 8 Future Work and Conclusion .....	77
Future Work .....	77
Supervisor .....	78
Energy Source Adapter .....	79
HyPER Load Adapter.....	79
Conclusion .....	80
Bibliography.....	82
Appendix A. Inductor Design Parameters .....	85
Appendix B. Bidirectional Converter Schematics, Parts List, and PCB Layout.....	88
Appendix C. SIMULINK® Simulations.....	95
Appendix D. dSpace Controller and Interface .....	104

## LIST OF FIGURES

Figure 1.1: Proposed hybrid architecture .....	3
Figure 2.1: Talon® stair climbing power profile .....	7
Figure 2.2: Basic boost converter topology .....	9
Figure 2.3: Synchronous boost converter topology .....	9
Figure 2.4: Estimated inductor losses .....	11
Figure 2.5: Completed inductor .....	12
Figure 2.6: Converter control circuitry .....	13
Figure 2.7: Simple converter schematic.....	14
Figure 2.8: Predicted converter losses .....	15
Figure 2.9: Predicted converter efficiency .....	15
Figure 2.10: Complete converter .....	17
Figure 3.1: HyPER system topology .....	18
Figure 3.2: Talon® stair climbing profile.....	21
Figure 3.3: Talon® power frequency spectrum .....	22
Figure 3.4: Filter frequency response .....	23
Figure 3.5: Low frequency power spectrum .....	23
Figure 3.6: High frequency power spectrum .....	24
Figure 3.7: Simple HyPER system representation.....	25
Figure 4.1: HyPER system SIMULINK® model .....	28
Figure 4.2: Controller power command comparison .....	31
Figure 4.3: Bus capacitor simulation results.....	32
Figure 4.4: Battery simulation results .....	33
Figure 4.5: Ultracapacitor simulation results.....	33
Figure 4.6: Hyper system SIMULINK® model with compensation .....	35

Figure 4.7: Bus capacitor simulation results with compensation.....	36
Figure 4.8: Ultracapacitor simulation results with compensation.....	37
Figure 5.1: Scalable HyPER system representation.....	39
Figure 5.2: HyPER control system representation.....	43
Figure 5.3: Simplified HyPER control system representation.....	44
Figure 5.4: SIMULINK® control system simulation.....	50
Figure 5.5: Simulation energy states, $kpc = 0$ .....	51
Figure 5.6: Simulation energy states, $kpc = 0.05$ .....	52
Figure 5.7: System root loci, $5 \leq ki \leq 1000$ .....	53
Figure 5.8: System root loci, $5 \leq ki \leq 1000$ .....	53
Figure 5.9: System root loci, $75 \leq kp \leq 600$ .....	54
Figure 5.10: System root loci, $0.0001 \leq kpc \leq 0.1$ .....	54
Figure 5.11: System root loci, $0 \leq \omega_0 \leq 0.1$ .....	55
Figure 6.1: Converter testing variables, $Vin = 15$ .....	58
Figure 6.2: Converter testing variables, $Vin = 24$ .....	59
Figure 6.3: Converter testing variables, $Vin = 33$ .....	59
Figure 6.4: Converter efficiency, $Vin = 15$ .....	60
Figure 6.5: Converter efficiency, $Vin = 24$ .....	60
Figure 6.6: Converter efficiency, $Vin = 33$ .....	61
Figure 6.7: Converter efficiency vs. power, $Vin = 15$ .....	62
Figure 6.8: Converter efficiency vs. power, $Vin = 24$ .....	62
Figure 6.9: Converter efficiency vs. power, $Vin = 33$ .....	63
Figure 6.10: Converter loss breakdown.....	64
Figure 7.1: HyPER test bench.....	67
Figure 7.2: dSpace HyPER GUI.....	68

Figure 7.3: dSpace SIMULINK® control model.....	69
Figure 7.4: Talon® stair climbing power profile.....	70
Figure 7.5: Ultracapacitor energy for various $kpc$ values.....	71
Figure 7.6: Capacitor levels.....	72
Figure 7.7: Battery testing results.....	73
Figure 7.8: Ultracapacitor testing results.....	73
Figure 7.9: Bus capacitor testing results.....	74
Figure 7.10: Measured high and low frequency power profiles.....	75
Figure 8.1: Expanded HyPER architecture.....	77
Figure B.1 Converter power net schematic.....	89
Figure B.2: Converter control circuitry schematic.....	90
Figure B.3: Converter gate drive circuitry schematic.....	91
Figure B.4: PCB layout top layer.....	94
Figure B.5: PCB layout bottom layer.....	94
Figure C.1: Control system simulation main system.....	95
Figure C.2: Filter algorithm subsystem.....	96
Figure C.3: HyPER system simulation main.....	97
Figure C.4: PI controller subsystem.....	98
Figure C.5: Capacitor charge circuit subsystem.....	99
Figure C.6: Filter algorithm subsystem.....	99
Figure C.7: Lumped batter/generator model (battery charge mode).....	100
Figure C.8: Lumped battery/generator model (battery discharge mode).....	100
Figure C.9: Low frequency source subsystem.....	101
Figure C.10: Converter model subsystem.....	102
Figure C.11: Capacitor model subsystem.....	103

Figure D.1: dSpace SIMULINK® controller .....	104
Figure D.2: Device DAQ and monitoring subsystem .....	105
Figure D.3: Safety override subsystem .....	106
Figure D.4: Controller subsystem .....	107
Figure D.5: dSpace D/A interface subsystem .....	108
Figure D.6: Current command calculation subsystem .....	108

**LIST OF TABLES**

Table 5.1: Controller setpoints.....	56
Table 7.1: Supervisory controller set points .....	70
Table A.1: Inductor specifications.....	85
Table B.1: Converter passive device definitions .....	92
Table B.2: Converter active device definitions.....	93

## ACKNOWLEDGEMENTS

This thesis is based upon work supported by the Naval Explosive Ordnance Disposal Tech Division under Contract Number N00024-02-D-6604, DO#0501. The content of the information does not necessarily reflect the position or policy of the Government, and no official endorsement should be inferred.

I would like to thank Dr. Heath Hofmann for being a great advisor and guiding my academic work throughout the research for this thesis and other projects. Dr. Mayer, thank you for taking the time to review this work and serve on the thesis committee. To Dr. Karl Reichard and Chris Rogan, thank you for not only reviewing this thesis and overseeing the work on the accompanying project, but also for guiding and advising me in my first year working as an engineer.

## **Chapter 1**

### **Hybrid Power and Energy for Robots (HyPER)**

The current limiting factor in electric vehicle design and performance is the energy source. This problem has been recognized in the automotive industry, and while much research has gone into alternatives to batteries, or augmentation through a hybridization scheme, very little of this research has gone toward doing the same for robots. The research in the robotics field has focused mainly on integrating highly energy dense power sources with little thought applied to optimizing the efficiency of power converter designs and efficient energy management. There has been no effort to standardize the design of robot power systems through the use of a scalable power delivery architecture. The goal of the HyPER system architecture is to provide a power system architecture which can be applied to any size robotic platform and accommodate a variety of energy storage and generation devices. The system architecture also facilitates power source optimization and management which can extend the operating time/range of the robot, and extend the life of the energy storage devices.

#### **Currently Fielded Platforms and Uses**

Ground robots are often classified according to size: small, medium, and large. The exact weight definitions vary, but one example might be small, up to 80 lbs; medium, 80-120 lbs; and large, up to the size of passenger vehicles. Each class of robot has its own unique uses and thus a unique set of power and energy requirements.

One of the smaller robots used by the U.S. military is the SUGV 300® [14], made by iRobot®. This robot has several different configurations for different applications, including

surveillance and improvised explosive device (IED) disposal. It is designed to be particularly agile and mobile for use in rubble and narrow passages.

A robot representing the medium class is the TALON® [15] made by Foster-Miller. This robot is often used in IED and explosive ordnance disposal (EOD) and in surveillance operations. The original power system on the robot is a proprietary battery also manufactured by Foster-Miller.

Finally, the MULE® [16] made by Lockheed Martin is one of the largest unmanned ground vehicle platforms available. This 2.5-ton class vehicle comes in countermine, light assault, and transport variants. It currently utilizes a diesel electric drive train, so that as the appropriate technology becomes available, a hybrid system could be implemented.

There are many other robotic platforms in use today, but these three examples show the range in sizes and the applications of the current generation of robots. Most robotics applications could benefit from the use of a hybrid power architecture. Very small robots are the exception where the power demands are so low and the size is so small that multiple energy devices may be impractical due to space limitations. However, efficient energy management is still a requirement.

### **Hybrid Power and Energy Architecture Benefits**

Many robots can expand their utility when a hybrid power architecture becomes available. There are a number of scenarios where a hybrid architecture could be used to extend the operation time of the robot. For example, under silent watch conditions, a robot must complete its mission before energy source is depleted. If a diesel generator were integrated into a hybrid architecture on the robot, the batteries could be recharged in the field without the robot having to return. Beyond significantly improving operation time, a hybrid power architecture can benefit a robotic system through the implementation of health monitoring algorithms for each

energy device and for the system as a whole. This has the potential to extend the life of the devices. However, the most compelling argument for using a hybrid architecture is the commonality of energy storage devices. Currently, robots each have their own unique energy source, whether it is a generator or battery. If the proposed architecture were implemented, all robots would have the capability to use the same energy sources in the field. This would have a huge positive effect on the logistics required to supply the energy sources and the down time of the robots in case of power system failure.

### Proposed Hybrid Power and Energy Architecture

The proposed architecture is essentially identical to a series configured hybrid vehicle. The robot is connected to a common power bus, to which the energy sources are also connected, each through an interface. Each energy storage device interfaces to the main robot power bus via a DC-DC converter. Shown in Figure 1.1 is a representation of the proposed hybrid architecture.

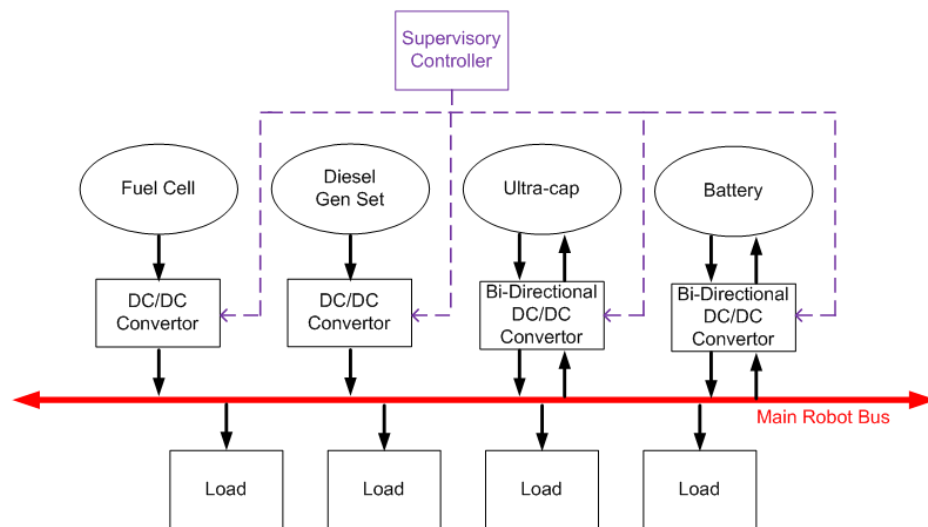


Figure 1.1: Proposed hybrid architecture

A significant benefit of a hybrid system is the ability to recapture energy that would otherwise have been wasted, through some regeneration scheme. Another advantage of a hybrid system is the ability to transfer power among the devices. For these reasons some devices will require a bidirectional DC-DC converter. Certain other devices, such as a fuel cell which can only source energy, require only a unidirectional converter.

No device can work in parallel with other devices without some type of coordination. The supervisory controller coordinates the interaction of the energy storage device. The goal of the supervisory controller is to provide the robot with a continuous constant voltage source through any power demand.

The bidirectional DC-DC converters operate as current sink/source modules; the supervisory controller sends the converter either a positive or negative current command, and the converter matches that command by transferring current into or out of the main robot power bus.

As the components of the proposed architecture are outlined in the following chapters, the benefits of a scalable hybrid power and energy system will be discussed more fully. This thesis will be focusing on the hardware design and the design and stability of a simple supervisory controller.

## **Summary**

Advances in robot performance have been limited by the lack of significant new advances in the mature field of battery technology. The focus of robotic power systems must expand from the use of single energy devices to the inclusion of multiple devices which can be optimized for a robotic platform. The challenge lies in the development of the hardware and control algorithms for a scalable power delivery architecture which satisfies the power and energy requirements of most unmanned ground vehicles. This thesis proposes an architecture which is

easily scalable and facilitates the use of a wide variety of energy storage/generation devices, while focusing on the system control algorithm and its stability. The experimental results for an example system are presented, demonstrating that the architecture functions properly when faced with real world robotic power demands.

## **Chapter 2**

### **Hardware Development**

The core of the proposed scalable power architecture is the bidirectional DC-DC converter. The converter interfaces the energy storage device to the main robot power bus and controls the power flow on or off of this power bus. The first step in the design is to select a preliminary robot platform, and determine the platform power and energy requirements. To ensure the architecture accommodates a wide range of energy sources a survey of currently and soon-to-be available technologies in the energy storage and generation field must be conducted to determine the input and output parameters of the converter. Once the input and output operating conditions have been determined, a converter topology may be selected. DC-DC conversion has been applied to similar applications, so the development of a new topology is not required. Rather, a common topology can be modified to fit the requirements of this particular application. As in any hybrid system, efficiency is key to the energy conversion topology, thus the major components in the circuit should be designed with this in mind. Finally, after the topology and design of the converter have been finalized, the efficiency of the converter can be estimated.

### **System Requirements**

As the goal of this project is to develop a scalable architecture for robot hybrid power systems, the actual robot on which it is developed is not important. Data has previously been collected for the Talon®, which is a medium (80-120 lbs) size robot that is widely used by the U.S. military. The data consists of approximately ten different tests conducted in a controlled environment by the Applied Research Laboratory (ARL). The tests ranged from driving the robot

around a test track until the batteries died, to driving it over obstacles with a large payload. Of all the test profiles which were run, one of the hardest on the robot was the stair climbing profile, shown in Figure 2.1. The OEM battery voltage and current were recorded for the duration of the test and then multiplied together to arrive at the power profile.

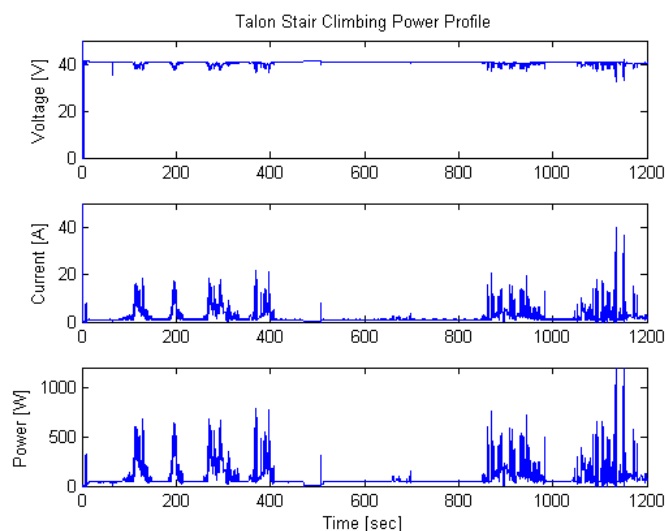


Figure 2.1: Talon® stair climbing power profile

The power profile, shown in the bottom subplot of Figure 2.1, contains a large number of peaks making it difficult for some energy sources to handle and ideal for the use of a hybrid system. While this particular robot's power demand generally does not exceed 600 watts and averages around 100 watts, occasionally the power can climb to 1.3 kilowatts. Since the hybrid system is designed to supply the power demand through multiple sources, a particular source will generally not have to supply the whole demand.

The bus voltage of the Talon® in the top subplot hovers just below 40 volts. It is not regulated, so it can change with battery state of charge and power draw. Considering this and the fact that 50 volts is generally considered the maximum safe voltage, the HyPER system bus voltage will be limited to under 50 volts with the exact number to be determined at a later time.

Assuming a voltage of 35 volts to be the lowest desired bus voltage, the maximum peak current the converter should ever have to supply is around 35 amps. Even in these cases it will be of fairly short duration. Designing the converter around the voltage and current parameters above, the converter should be capable of delivering approximately 1 kW.

### **Energy Source Parameters**

Before the topology of the converter can be determined, it must be known what energy sources are available for use. It is desirable for logistical reasons to use energy sources that are already available in the field, such as the BB2590 radio battery. This lithium ion battery has two nominally 14.4 volt strings of cells in a single package. These strings can be configured in either series or parallel, and a series configured battery has a fully charged maximum voltage of 31 volts. Other common batteries are vehicle batteries for 12- or 24-volt systems. A market survey was conducted to find other devices of appropriate voltage and power requirements. A number of ultracapacitors were considered, and those that could be safely deployed in portable systems ranged from 20-30 volts. The same applies to fuel cells and generators. To summarize, as almost all appropriate energy sources are designed for systems that operate at a nominal 28 volts, it can be assumed that all sources which would be used in the HyPER system have a lower voltage than the system bus voltage.

### **Bidirectional Converter Topology**

Setting the bus voltage higher than the voltages of the energy sources has the advantage that only a boost mode has to be considered in the design of the DC-DC converter. Another point to be considered is that all the energy sources are standalone devices and a single ground potential

can be used for all system energy sources. Thus the converter does not need to be isolated. A simple boost converter, as shown in Figure 2.2, would suffice if a unidirectional supply were needed. In a boost converter, energy is stored in the inductor during the first part of the switching cycle, during which the semiconductor switch is closed. During the second part of the switching cycle, the switch is opened, the diode is biased, and power flows from the inductor to the load. The diode in the circuit prevents any power flow in the reverse direction.

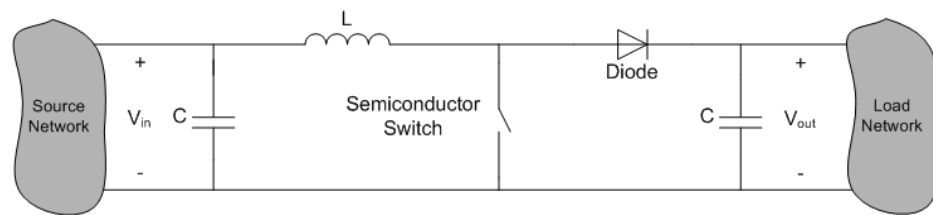


Figure 2.2: Basic boost converter topology

However, one of the most convincing arguments to hybridizing any system is that power can be recaptured from the environment. Another argument is that the health of an energy source can be maintained by transferring energy between the devices, such as a generator being used to charge batteries. In order for this architecture to facilitate the use of viable alternative power sources, it must be capable of bidirectional power flow. By replacing the diode with another MOSFET, shown in Figure 2.3, the switching of the converter can be completely controlled allowing power to flow in either direction.

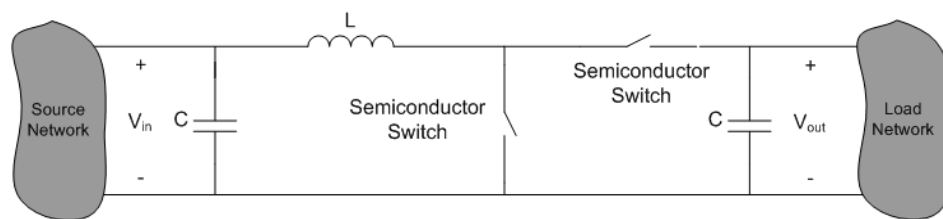


Figure 2.3: Synchronous boost converter topology

The idea of replacing diodes with MOSFETs is not new and has been used in a variety of applications, the most notable being that of the synchronous rectifier. This strategy is usually employed in high efficiency applications. The simplicity, efficiency, and controllability of the proposed circuit make the converter an excellent solution.

### Converter Component Design

As described in the previous section, the topology of the converter is that of a modified boost converter consisting of three main components, two MOSFETs and an inductor. The MOSFETs are readily available off the shelf and are appropriately sized for the voltage and current ratings of the converter. However, it is generally difficult to obtain properly sized power inductors. If a custom inductor were designed for the converter, not only would it be appropriately sized, it would also be possible to design it to be extremely efficient. The size of the inductor can be determined by manipulation of the fundamental inductor equation.

$$V_L = L \frac{di_L}{dt} \quad 2.1$$

Where  $\frac{di_L}{dt}$  is approximated using  $\frac{\Delta I}{\Delta T}$ . Using a switching frequency of 100 kHz, a maximum of five amps ripple, and a voltage difference of fifteen volts; the inductor size was estimated to be 30 $\mu$ H.

The two main losses in an inductor are core losses and conduction losses. Core losses are determined by the material properties of the core. For this inductor it was decided that the high efficiency Molypermalloy toroidal cores would be used as these cores have traditionally been some of the most efficient on the market. It is even more important to minimize the conduction losses in the inductor which can easily be an order of magnitude higher than the core losses.

Although not extremely high, the desired switching frequency is high enough to make skin effect

in the conductors significant. The use of Litz wire, a wire composed of a bundle of many much smaller wires, solves this problem. This allows the size of each wire within the bundle to be small enough that the entire wire is used for conduction not just the outer skin. Thus the AC resistance of the inductor is minimized. The calculations for the inductor design and its estimated losses can be found in Appendix A. The estimated conduction losses of the inductor are shown below in Figure 2.4.

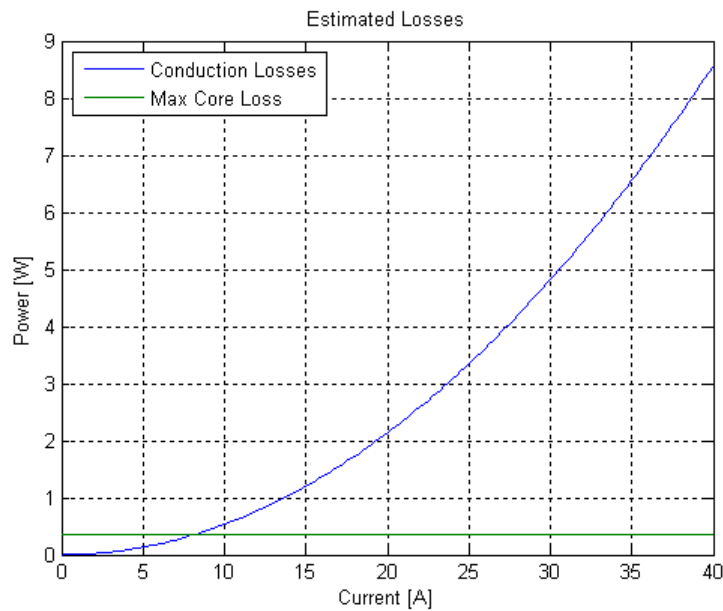


Figure 2.4: Estimated inductor losses

Assuming that the converter is transferring 1kW, the inductor losses would be less than 1% of the total power. The resulting inductor, shown in Figure 2.5, has an inductance of 60 $\mu$ H and a DC resistance of 7m $\Omega$ . The resulting inductance is higher than the estimated need of 30 $\mu$ H and can be accounted for by the conservative assumptions built into the inductor design process.



Figure 2.5: Completed inductor

### Control Circuit

The main components of the circuit have now been designed with the exception of the control circuitry. Essentially each converter acts as a current sink or source, as seen by the main power bus. The supervisory controller should be able to command the converter as to how much current to provide to the bus, and the converter should then provide that current. These requirements lend themselves to using an on-board analog closed-loop controller to control the duty cycle of the MOSFETs. There is one state on the converter; the inductor current. It makes the most sense to control the inductor current, as states tend to be continuous and to change more slowly than a random variable, such as the output current, which transitions between zero and some high current when the upper MOSFET is switched. By placing a current sensing resistor in the path of the inductor current, the current can be measured using a differential amplifier and used as an input to the analog controller. However, placing the resistor in the direct path of the inductor current could potentially cause measurement problems as the measurement's reference would be floating at the device voltage. By placing the sensor in the return path, which is shown

in Figure 2.7, the negative of the inductor current can be measured at the neutral potential of the system. The topology of the differential amplifier and PI controller is shown in Figure 2.6.

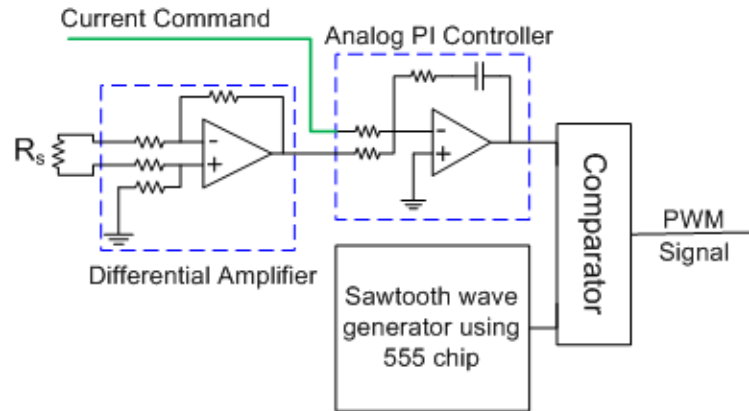


Figure 2.6: Converter control circuitry

The measured current and the reference current are summed at the input to the Proportional-Integral (PI) controller to generate an error term. This error term is passed through the PI controller to generate a control signal. The control signal is compared to a sawtooth waveform to generate a PWM signal which can then be used as a command for the gate drive circuits.

### Complete Circuit

The design of the major circuit components has been described. While there are other components to the circuit, they are commonplace and can be found in numerous references. A simple circuit schematic is shown in Figure 2.7. Complete schematics and a printed circuit board layout can be found in Appendix B.

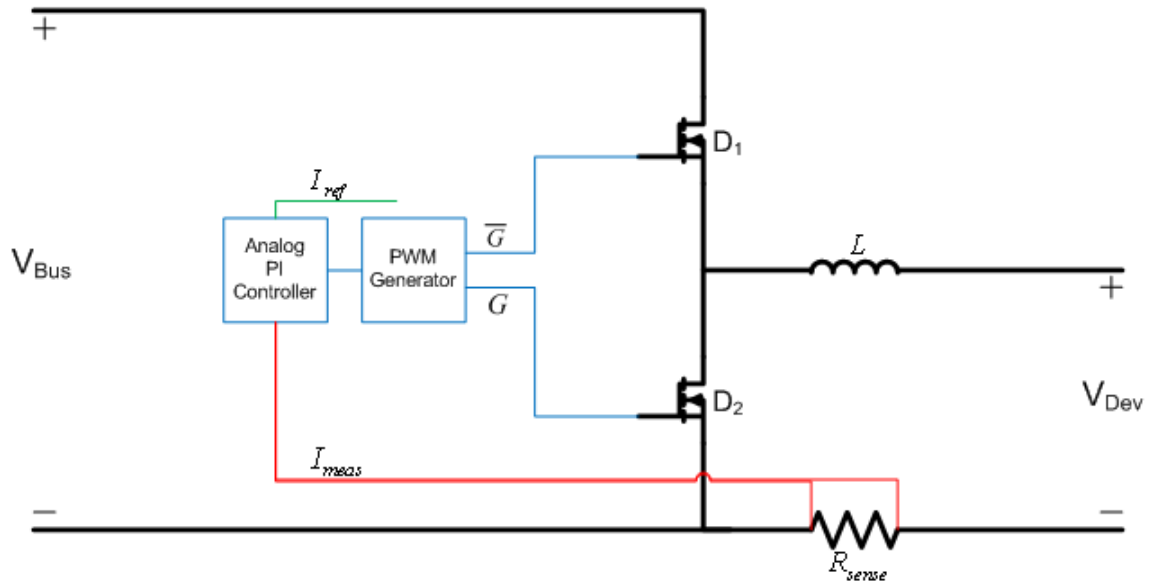


Figure 2.7: Simple converter schematic

### Converter Efficiency

In order to determine the converter performance we must accurately model the losses. For this particular converter, the losses are comprised of conduction losses, switching losses, and control and drive circuitry losses. The conduction losses will likely be the most significant as they will be proportional to the square of the current. The switching losses are proportional to the current through the MOSFETs, and the control circuitry losses should be relatively constant. The predicted losses are shown in Figure 2.8.

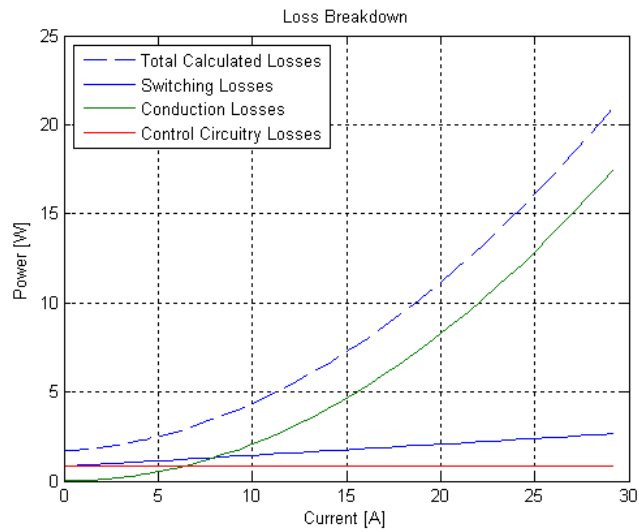


Figure 2.8: Predicted converter losses

As expected, the conduction losses dominate the total losses of the converter. In terms of the total efficiency, however, the converter should be extremely efficient. The efficiency of the converter depends on the input voltage as can be seen in Figure 2.9, where the lower the voltage, the more current must be transferred which increases the losses relative to the amount of power transferred.

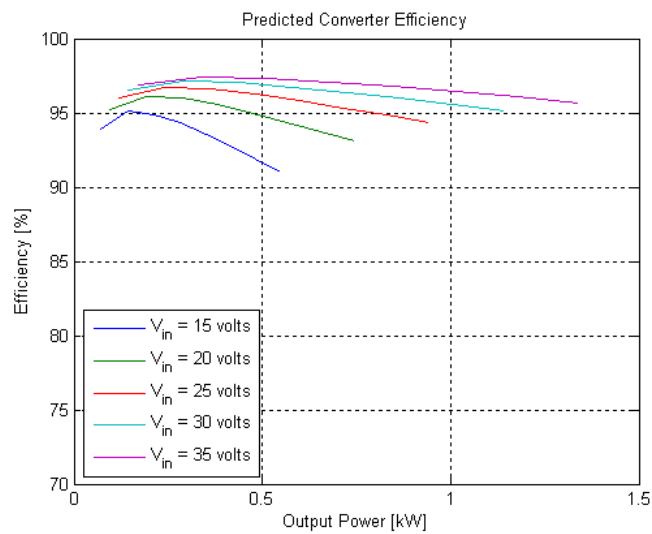


Figure 2.9: Predicted converter efficiency

Because of this, it is preferable to have the source voltages as close as possible to the bus voltage, in order to minimize the current required to meet the power demands. A more in depth description of the modeling and the empirical efficiency of the converter will be further discussed in a later chapter.

### **Summary**

This chapter covered the design of the bidirectional DC-DC converter which interfaces the energy devices to the robot power bus. The hardware was designed around the Talon® robot, and the robot's power and energy requirements were determined using previously recorded power data. A summary of the range of devices expected to be used in the system were covered. It was found that the devices generally had a lower voltage than the robot power bus, allowing the use of a simple boost converter. To achieve a bidirectional power flow, a diode in the boost converter was changed to a MOSFET. This modification has been used previously in synchronous rectification to boost efficiency, but also allows complete control of the power flow in both directions. In order to increase the conversion efficiency, all the inductor was custom designed for this application. An on board PI current regulator regulates the power flow to a commanded reference. Finally, the losses of the converter were estimated and a preliminary converter efficiency was plotted. The completed converter is shown in Figure 2.10 with a BB390 in the background for size comparison. In future revisions of the board it will be possible to make the converter more compact.



Figure 2.10: Complete converter

The HyPER architecture will utilize multiple DC-DC converters which will work in parallel to supply the main robot power bus. Though each converter has an individual analog current regulator on board, this is not sufficient for a coordinated operation. In the next chapter the parallel combination of the converters will be considered.

## Chapter 3

### Supervisory Controller Development

In the last chapter the design of a bidirectional DC-DC converter was discussed. In order to implement these converters in a power delivery system, there must be a supervisor coordinating the converters. Figure 3.1 shows the relationship between the energy sources, the converters, the supervisory controller, and any loads present in the system.

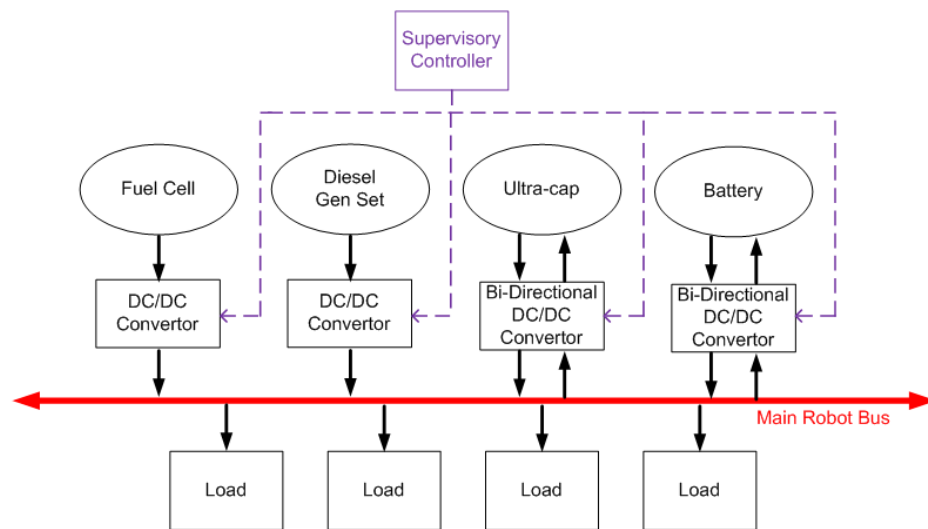


Figure 3.1: HyPER system topology

There are essentially two layers of control that must be implemented in the supervisory controller for the hybrid architecture to be viable. A low-level controller must be able to regulate the energy on the main robot power bus by generating current commands for every converter in the system. Secondly, a high-level controller must manage the devices themselves, making decisions on which ones are in use, and manage the payloads along with various other tasks. The controller developed within this chapter will use only two energy storage devices. However, it

will be shown that the number of storage devices in the system can be easily expanded. By the end of the chapter a low-level control system will be proposed.

### **High-level Controller Requirements**

To describe and analyze the full high-level system controller is beyond the scope of this thesis. However, some of the more rudimentary functions will be described. At the highest level, the supervisory controller's purpose is to optimize the performance of the system for any given operating conditions. This could include a high power, fast acceleration mode if speed is of the essence. It could also include a low power, high efficiency mode if operating conditions of the robot demand long endurance. How one approaches the control design will have significant impact on any of these conditions. Many different controllers could be preprogrammed in the supervisor, each one tailored to a particular set of operating conditions. However, with the infinite possible combination of conditions that the system could experience, this would be a rather impractical approach. Thus, there must be one overarching controller which is a good compromise for any situation.

The high-level controller has four main functions. First, it has to configure the low-level controller at any time during operation. Second, it has to monitor the devices, which includes ensuring all devices are within safety limits, calculating state of charge (SOC), and recording real time current and voltage. The controller must also be able to control devices based on the overall system's state of charge, or on a particular mission's energy requirements. In the case of the BB2590 batteries, it must be able to place them in a charge mode if the SOC drops too low. If there are any devices in the system which are not active at all times, such as a generator or fuel cell, the supervisory controller must have the capability to activate them. When a device

activates, deactivates, or changes operation mode, the supervisory controller must reconfigure the low-level controller appropriately.

Beyond these main functions, other potential applications for the supervisory controller could include health monitoring algorithms, energy optimization algorithms, mission energy requirement estimation, mission planning, and mission programmable operation modes.

### **Low-level Controller Requirements**

The HyPER system is a hybrid system and by definition must consist of multiple devices. To optimize the efficiency of the system the characteristics of the devices should be considered. How should the controller decide what device sources the energy? For the purposes of this thesis we only consider two energy sources, the BB2590 lithium ion battery and an ultracapacitor. Using these two devices it is possible to develop a method to manage the system energy and to demonstrate the capabilities of the low-level controller while maintaining some level of simplicity.

The BB2590 is optimized for relatively low power high energy applications such as radios and weapon systems. While it is excellent for providing low power for a long period of time, it has disadvantage of having a high series resistance. During periods of high power draw, the losses increase greatly thus making it inefficient for the large surges demanded by the robot power profile shown in Figure 3.2.

Ultracapacitors have become increasingly popular in the last few years, and, depending on the size, have been used in over-the-road trucks for use during starting, energy sources for rail guns, and supply banks for radar and sonar systems. They are designed to handle high power short duration pulses. Though the energy contained in an ultracapacitor can be depleted rather

quickly, it has the advantage of having a very low equivalent series resistance (ESR) making it very efficient when used to supply peak loads.

The power profile of the Talon® has an average power of less than 100 watts, but the peak draw is an order of magnitude higher. If these power surges are drawn from a battery the losses will also be very high. If the entire profile is drawn from an ultracapacitor, the energy will be depleted very quickly.

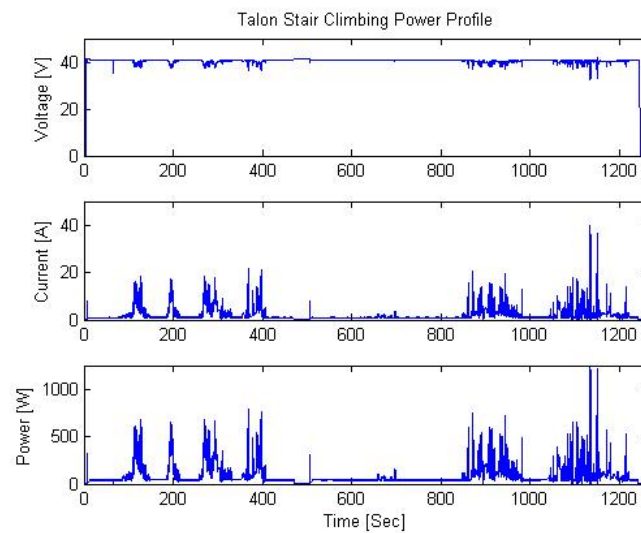


Figure 3.2: Talon® stair climbing profile

Intuitively looking at the power profile, it would be preferable for the battery to supply the DC power or the low frequency high energy portions; and the ultracapacitor to supply the higher frequency, high power portions of the profile. Basing the power allocation upon the frequency content of the power demand is easily implemented through the use of a filter which can be optimized to the frequency range of the energy devices. Before proceeding further the frequency content of the power profile, shown in Figure 3.3, must be analyzed. The frequency spectrum in the bottom subplot is zoomed to emphasize the high frequency components of the profile. The DC component, which cannot be completely seen, has a magnitude of 83 watts. All the significant

components of the power spectrum occur below 100 Hz. Most significant components actually occur below 25 Hz.

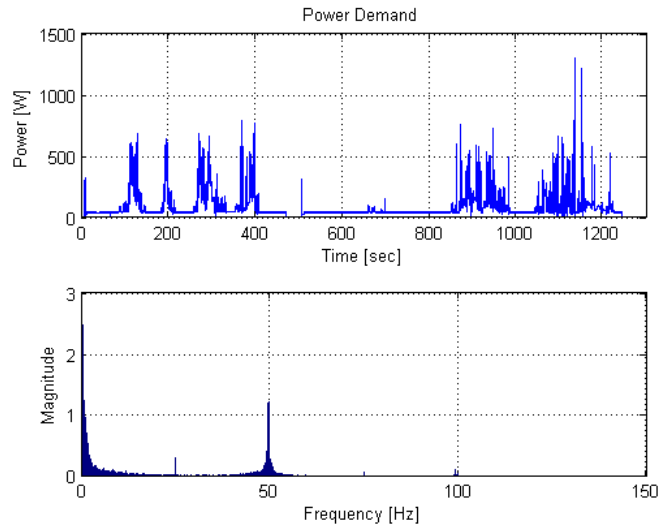


Figure 3.3: Talon® power frequency spectrum

However, there is an anomaly in the Talon® data. There is a significant amount of power around 50 Hz with harmonics at 100 Hz and 150 Hz. These unexplained frequency components occur in all the Talon® data, regardless of its operating conditions, and are not present on any other platform. The filter used for the power allocation is a first order filter with a corner frequency of 0.1 Hz, and its frequency response is shown in Figure 3.4.

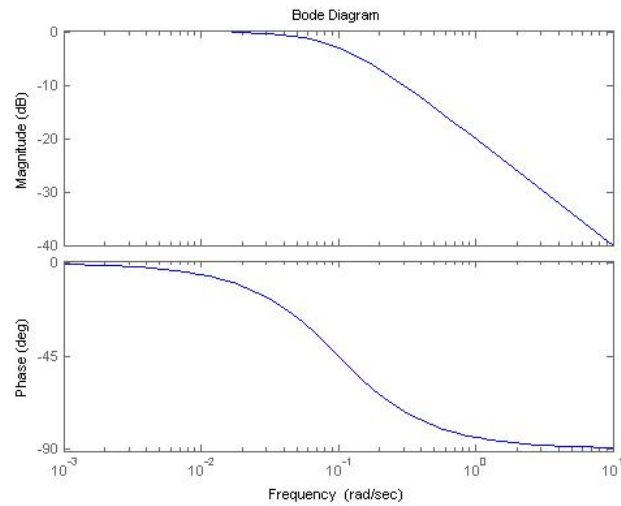


Figure 3.4: Filter frequency response

The low frequency components of the profile, the portion supplied by the battery, are shown in Figure 3.5. Although there are still significant surges of power, these demands are relatively long, on the order of twenty or thirty seconds. The amount of energy required is still too high for an ultracapacitor to supply. The energy plot does not include the DC energy. Even without the DC component, the amount of energy required by the low frequency power demand is approximately 10kJ.

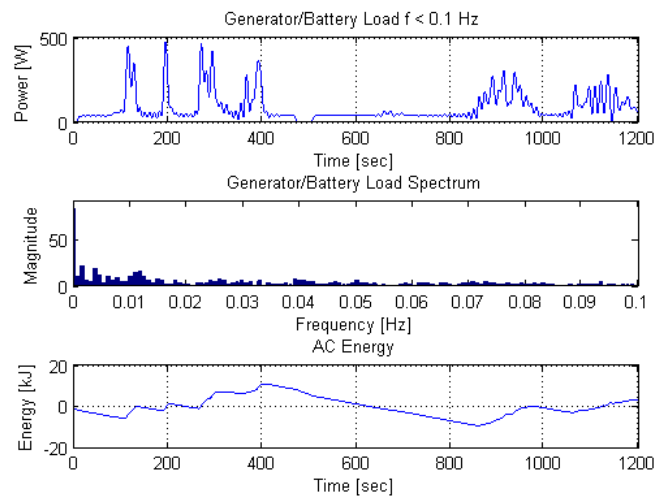


Figure 3.5: Low frequency power spectrum

Figure 3.6 shows the high frequency demand, which the ultracapacitor is expected to supply. By looking at the scale on the magnitude, it can be seen that the amount of energy required is an order of magnitude less than the low frequency portion of the profile. It can be expected that a reasonably sized ultracapacitor could supply this amount of energy.

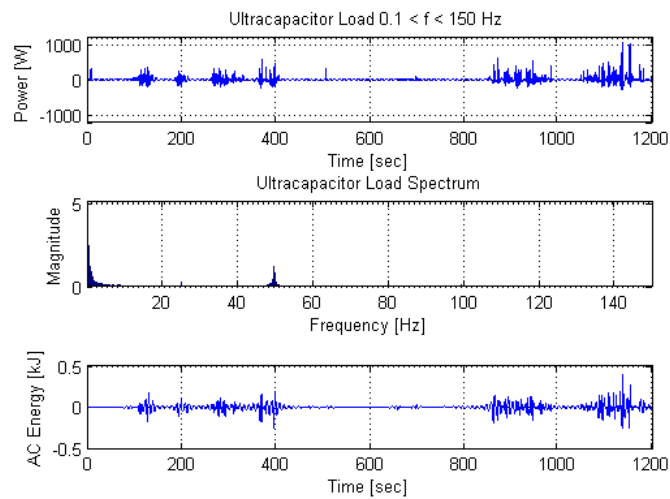


Figure 3.6: High frequency power spectrum

The purpose of generating the current commands is ultimately to regulate the main robot power bus voltage. The state of the bus capacitor, its voltage, has no direct correlation to the power flowing through the bus. The energy of the bus has a constant direct connection to the bus voltage given by

$$E = \frac{1}{2}CV^2 \quad 3.1$$

The bus energy also has a direct relationship to the power flow. Because the architecture is a power system, it makes the most sense to control the bus energy rather than the bus voltage. The

bus energy will be used to generate a power command by passing it through a PI controller. The system is now a closed loop system and can be represented by the schematic shown in Figure 3.7.

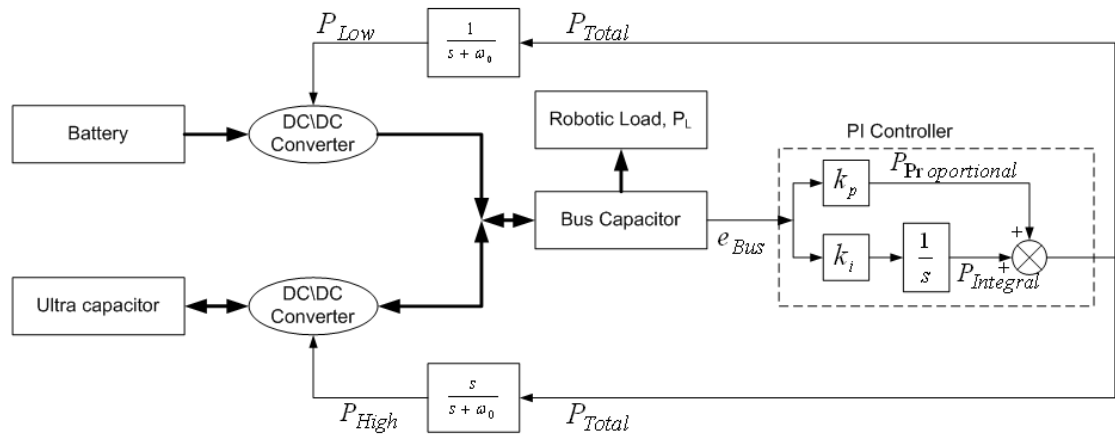


Figure 3.7: Simple HyPER system representation

There are three parameters which can be manipulated to optimize the performance of the system. The first two,  $k_p$  and  $k_i$ , are the PI controller's proportional and integral gains respectively. The last parameter is the filter corner frequency,  $\omega_0$ . This completes the components of the low-level supervisory controller. It does not, however, mean that the controller is complete.

In this chapter the low-level supervisory controller is developed for two devices, a battery and an ultracapacitor. The most important feature of this controller is that it can be implemented on multiple devices and is not limited to two. As shown in Figure 3.7, the filtering algorithm is depicted using a lowpass and a highpass filter. Adding a third or fourth device would require the power command to be filtered into three or four portions respectively. Using bandpass or highpass filters could be problematic as certain frequencies could be artificially accentuated, attenuated, or lost, and the filters are more complicated and computationally intensive to implement in a real time embedded system. For these reasons the filtering algorithm will be implemented using only low pass filters. Starting with the lowest cutoff frequency and proceeding to the highest cutoff frequency, any filter type and range can be achieved, and as a result the

system can be easily expanded to accommodate multiple energy sources. Depending on the frequency characteristics of the energy source, it may be necessary to use a higher order filter than the first order filter used in the previous example.

### **Summary**

A two level control strategy was proposed for the hybrid architecture. The functionality of a high-level smart controller, which monitors the energy source parameters and is able to control any operational modes, was quickly outlined. It was not fully developed and will not be covered further in this thesis. The function of the low-level controller was described and a topology of the controller was developed. It was shown that a feedback controller using the energy state of the bus capacitor would be sufficient for the system. The power command generated by this feedback controller is then filtered to split it into appropriate demand for each of power component. The filter specifications are set by the characteristics of the storage devices. The outputs of the filtering algorithm are the commands which are sent to the individual converters. The converters then transfer the appropriate power onto, or off of, the power bus. Though the system was developed for only two energy storage devices, the architecture can be scaled to accommodate multiple additional devices. Conceptually, the low-level controller has been developed, but it has yet to be shown that the control strategy can be implemented, can regulate the bus energy, or that the system is stable when feedback is applied. This will be accomplished in the next chapter.

## **Chapter 4**

### **HyPER System Simulation**

The supervisory control architecture was developed in the last chapter. In this chapter a model is developed for the HyPER system including the low-level supervisory controller. Blocks for energy storage devices are developed using their electrical characteristics, and a converter model is based on empirical data collected through hardware testing. The data acquired for the Talon® robot is used to simulate the load on the system. The simulation of the HyPER system will indicate if any problems exist with the control architecture. Any problems will become apparent in the simulation data presented in this chapter.

#### **System Model**

Shown in Figure 4.1 is the model of the HyPER system in a SIMULINK® block diagram. Before the models for the sub-blocks are developed several assumptions are made about the system to simplify the simulation. Assuming that the low frequency energy storage device is an infinite energy storage device, allows the system to operate in one continuous mode. The simulation and proof of stability of a system becomes much more difficult if discrete state switching occurs. This would have occurred had the battery been allowed to deplete its energy resources, and a generator switched in to charge it. This assumption will be discussed more during the development of the lumped ‘Battery/Generator Model.’

One key difference between the physical system and the simulation is that the current command is not sent to the DC-DC converter. It is sent to the associated energy storage device. The next few sections will outline the modeling of each device.



### **Lumped Battery/Generator Model**

To circumvent the discrete state switching problem the battery and generator will be lumped into one single model. To the rest of the HyPER system the model appears as a power source. Internal to the model there is discrete state switching between a battery charge and a battery discharge mode. However, for this simulation it is not really needed or utilized. In order to develop a fuller simulation, a battery and generator model would have to be developed to make the battery charge mode valid. This would add little to the understanding of the system, and was done only to show that there was room for further development in the model. Thus, for the purposes of this simulation, the battery is modeled as a constant voltage source that can sink or source whatever amount of power or energy is desired with no penalty applied for the high series impedance. This assumption can be justified if the amount of energy in each device is considered. A battery can store an order of magnitude more energy than an ultracapacitor. A generator is even more extreme in that it can be refueled any number of times and continue to provide energy as long as there is fuel to run. For the purposes of this simulation the generator is not used.

### **Capacitor Model**

An ideal capacitor is modeled as an integrator. This model can easily be expanded to include internal losses by modeling them as a resistance in series with the ideal capacitor. This resistance is known as an equivalent series resistance. An ideal capacitor with an equivalent series resistance (ESR) can be described by the following equation.

$$v = \int \frac{i}{C} dt + ir_{esr} \quad 4.1$$

There are more sophisticated capacitor models that model the parasitic losses within the capacitor. Although it has been shown that the model described in equation 4.1 is not adequate to describe the intricate internal operation of the ultracapacitor, it is sufficient for an overall system model. This model is used for both the bus capacitor and the ultracapacitor. The model allows the tracking of the energy sourced to the robot, the energy lost in the equivalent series resistance, the instantaneous power, the voltage, and current.

### **Converter Model**

The converter is modeled as a lumped power conversion device. It is not a detailed model based on the equations of the circuit. Rather, the model is based on the empirical data obtained through the experiments described in Chapter 6. Essentially it is just an efficiency block that calculates the amount of current being sourced to the bus. Its inputs are energy storage device voltage, device current, and bus voltage. Based upon these variables the converter model calculates the corresponding bus current. Finally, the converter uses a look-up table to calculate the converter's efficiency based on experimental results of the converter testing. This efficiency table takes into account both positive and negative power conversion.

### **Simulation Results**

Shown below are the results from the simulation of a portion of the Talon® robot stair climbing power profile. Figure 4.2 shows the performance at the output of the HyPER system.

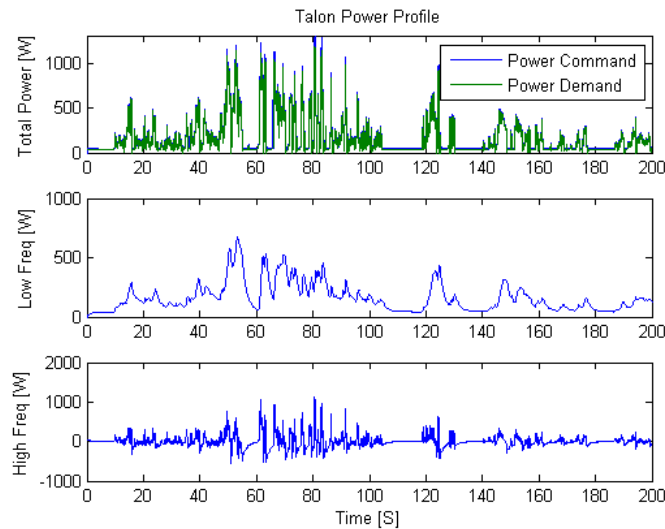


Figure 4.2: Controller power command comparison

This is one of the more important figures showing the results of the simulation. In the top subplot the output of the HyPER system's main regulating controller is shown. On top of the controller output is overlaid the power demand of the robot. This plot shows that the Proportional-Integral (PI) controller is generating a total power command appropriate to the load placed upon the system. It can also be seen from the two lower subplots that the filtering algorithm appears to be working. The middle subplot shows the low frequency power command, which is sent to a battery or some other low frequency devices. The bottom subplot shows the high frequency power command which is sent to a high frequency device in this case an ultracapacitor. This figure demonstrates that the PI controller combined with a filtering algorithm can be used to generate the robot's power command.

Figure 4.3 shows the variables associated with the bus capacitor. The top subplot shows the voltage at the terminals of the bus capacitor. This voltage has an error of less than 0.5 volts on either side of the set point. The voltage shows the output of the HyPER system, though it is not the variable which is being regulated. The energy in the bus capacitor is the control variable, and can be seen in the bottom subplot. The energy has a maximum error of one joule. This shows that

the main PI regulation loop is capable of maintaining the output voltage under a variety of load scenarios. These two figures show that the approach that has been taken to controlling the HyPER system is a valid approach.

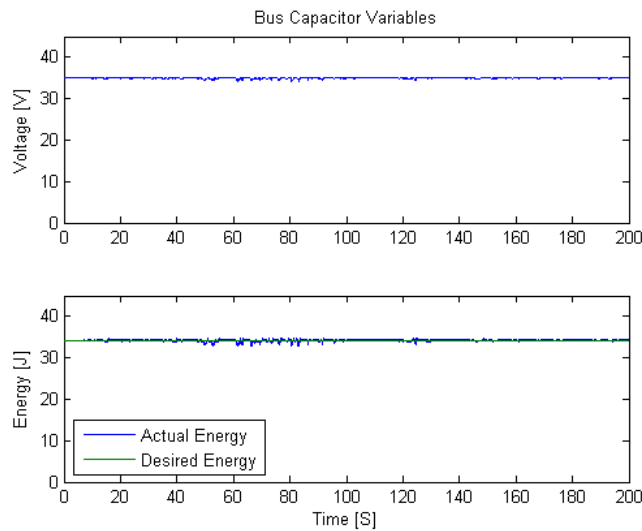


Figure 4.3: Bus capacitor simulation results

Figures 4.4-4.5 show the simulation results of the energy storage devices present in the system. Figure 4.4 shows the results from the battery. The battery voltage in the top subplot is artificially held constant, while in a real battery the voltage would decrease during periods of high demand. The middle subplot shows that the current being drawn from the battery contains relatively low frequency components. The bottom subplot in the figure shows the power drawn from the battery. This is only a scaled version of the current since the voltage is being held constant.

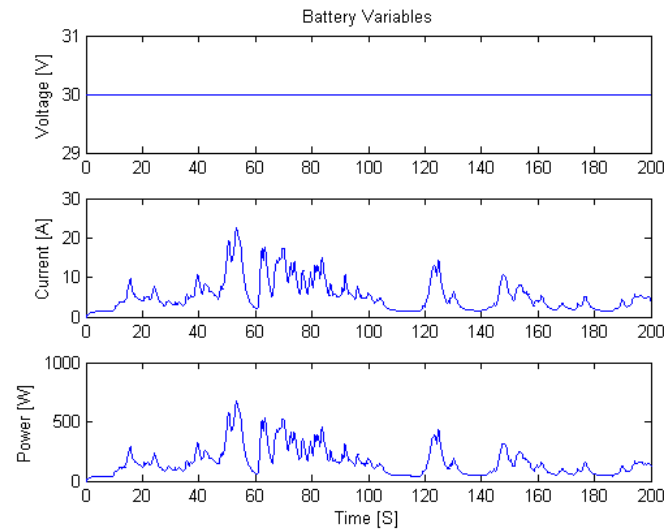


Figure 4.4: Battery simulation results

Figure 4.5 shows the results of the simulation for the ultracapacitor. The top plot shows the ultracapacitor voltage. The energy shown in the bottom subplot reveals an unexpected trend.

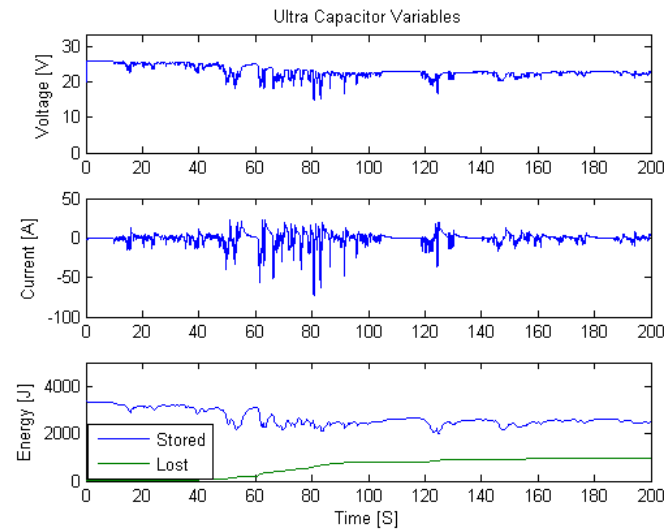


Figure 4.5: Ultracapacitor simulation results

The energy stored in the ultracapacitor declines significantly over the course of the simulation, which was only run for 200 seconds. Extrapolating the trend out to the length of an actual robot mission, the energy in the ultracapacitor would be completely spent after a very few

minutes. Where is this loss coming from? A capacitor is only capable of supplying current to non-DC loads. Theoretically, the way the ultracapacitor is being operated in the HyPER system, it should only be subjected to periodic loads on account of the filtering algorithm. This would be true if the system was ideal and there were no losses. The losses in the ultracapacitor are relatively insignificant and should not contribute enough to account for the amount of decay in the energy levels. The losses in the converter, however, are significant enough to account for the trend. Essentially, the losses in the converter are causing more energy to be drawn from the ultracapacitor than is being replaced. This decay cannot be ignored in the operation of the HyPER system, though it can easily be remedied by the addition of another control loop around the ultracapacitor alone. The SIMULINK® model with this control loop implemented can be seen in Figure 4.6.



In Figure 4.6 the block labeled ‘cap charge circuit’ contains a proportional controller for regulating the energy stored in the ultracapacitor. This is a very slow controller and is not meant to regulate the energy in the ultracapacitor tightly, as this would defeat the purpose of keeping an ultracapacitor in the system. In the case of a tight, control the battery would have high frequency components drawn from it to recharge the ultracapacitor. The battery would then be subjected to exactly the same profile as it would without the ultracapacitor in the loop. The control loop is only meant to offset the losses in the system, and keep the ultracapacitor from being completely depleted.

The simulations were rerun with this slow controller in the loop and the results show a marked improvement. Only the bus capacitor and ultracapacitor plots, Figure 4.7 and Figure 4.8 respectively, will be shown. Figure 4.7 shows the bus capacitor variables and demonstrates the results are similar to those in Figure 4.3. The output stability was not effected by the addition of another controller. From Figure 4.8, it can be seen that the controller offsets the decay, and the energy is not depleted as in the previous simulation.

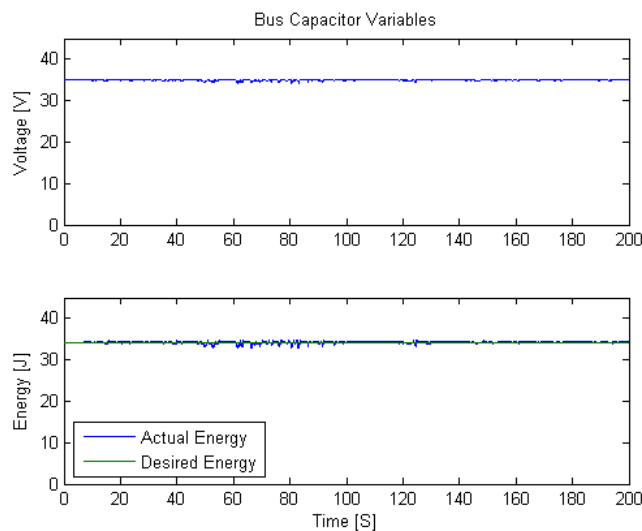


Figure 4.7: Bus capacitor simulation results with compensation

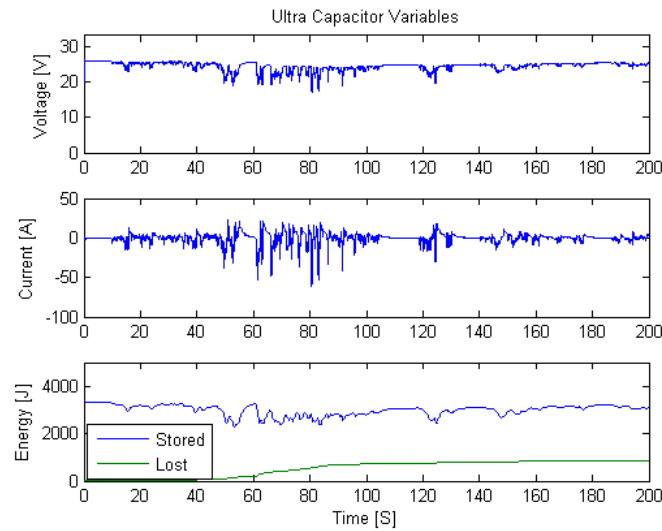


Figure 4.8: Ultracapacitor simulation results with compensation

### Summary

In this chapter, a model of a simple HyPER system was developed, including models for each energy storage device. The low frequency device was modeled as a very simple constant voltage model, while the high frequency device and bus capacitor models were based on the fundamental capacitor equation. The converter was modeled by its losses, which were determined from data gathered through the testing of the hardware, which is covered in a later chapter.

Using these models, the system was simulated using a power profile from the Talon® robot as a load. As initially proposed, the low-level controller was insufficient to maintain the energy levels within the system. The simulations of the system, which incorporated the modified controller, indicate that the control architecture is capable of regulating the bus capacitor energy and maintaining the energy stored in the ultracapacitor.

## **Chapter 5**

### **Supervisory Controller Stability Analysis**

In the last chapter, the modeling and simulation of the entire system was described, and the simulation results showed that the system would operate as desired. But before it is placed in a physical system, it should be analyzed to show that it is stable over the expected operating range. In this chapter the stability of the HyPER system is examined. A candidate analysis method consists of the simplification of the controlled HyPER system model using a number of assumptions about the system, its components, and the load. This simple model is then analyzed for stability.

Shown in Figure 5.1 is a general depiction of the HyPER system's scalable architecture. Though the architecture is intended to accommodate multiple devices, it is assumed for the purposes of the control analysis that only one low frequency source and one high frequency source is used. Though the analysis will be accomplished using only two energy sources, it is shown that the analysis is readily extendable to more energy sources.

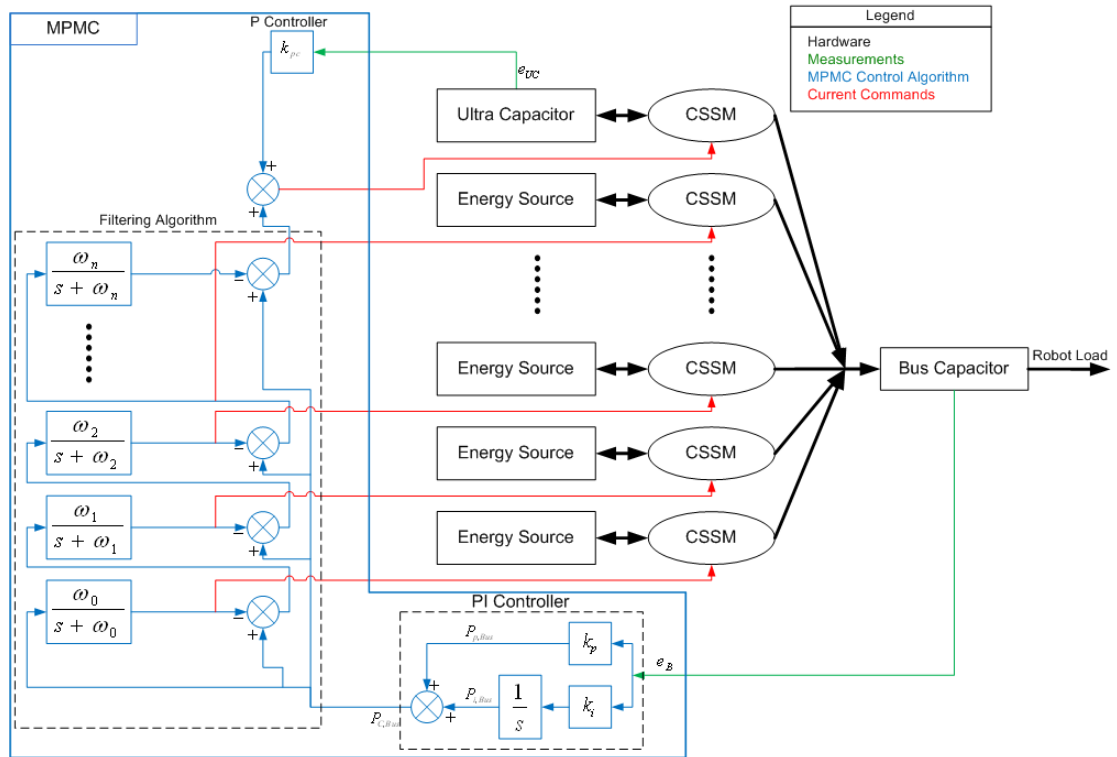


Figure 5.1: Scalable Hyper system representation

### Candidate Analysis Methods

There are a variety of ways to analyze the stability of a system. In simple systems, linear control theory can be used. However, most systems do not fall into this category without some manipulation. If the system can be modeled using the linear control theory, a mathematical model of the system is formed. This mathematical model is then represented in statespace equation form as shown in equation 5.1.

$$\dot{x}(t) = Ax(t) + bu(t)$$

$$y(t) = Cx(t) + du(t)$$

5.1

where  $A$ ,  $b$ ,  $C$ , and  $d$  represent system matrices. A system which can be manipulated into this form can be analyzed for stability by examination of the  $A$  matrix. If the eigenvalues of the matrix lie in the left half of the complex plane, then the system is considered stable.

For more complex systems Lyapunov control theory is often used. This involves using the states of the system to derive an energy equation. If it can be shown that this energy equation is positive definite, and that the derivative of the energy equation is negative definite, the system is considered asymptotically stable.

Initially, a Lyapunov function was to be derived for the system. However, this proves to be problematic when the efficiency of the converters is taken into account. A Lyapunov function also does not have a way to address the derivation of an energy equation for energy states. A close look at the system was then taken to see if it would be possible to manipulate it into a form which would allow an analysis using linear control theory. It was found that if certain assumptions are made, it is possible to model the system as a linear time invariant (LTI) system. Using the power flow it is possible to derive linear expressions (under certain assumptions) for the energy states of the system.

### **System Model Assumptions**

In order to simplify the system several assumptions need to be made. The first assumption is that the power supplied by the converter and the power commanded to the converter is identical. This also assumes that the power commanded is within the capability of the energy source. Residing on each DC-DC converter is an analog current regulator. This regulator ensures that the commanded current and supplied current are identical. Regulation is not instantaneous, however, using a two time scale approach it can be assumed that it is. The step response of the current regulator is under  $20 \mu\text{sec}$ , which is much faster than the response of the

outer control loop. Thus, in the “slow” time scale the two currents, and thus the powers, can be considered the equal.

Second, it is assumed the losses in the system can be neglected. The largest loss of the system is located in the converter. As for any system, the energy conversion devices should be designed such that they primarily operate at peak efficiency. For the purpose of this analysis, it is assumed that the converter is always operating near that peak. This peak efficiency is sufficiently close to 100% to neglect the losses in the converter. Additionally, there is another argument which can also be used. In this analysis there are no assumptions made about the robot power demand. Therefore rather than associating the power losses with the converter, it can be assumed that the converter is 100% efficient, and that the power demand on the ultracapacitor contains both the high frequency power command and a disturbance equal to the power losses in the converter. Though the disturbance will not be modeled here, it is possible to place some restrictions on it. It is guaranteed to be positive, that is drawn from the ultracapacitor. This restriction can be placed upon the disturbance as energy cannot be created by the converter.

The second loss is the loss associated with the energy storage device itself. However, this loss does not really affect the system stability, but reduces the total energy available to the system. These losses are generally considered small enough to be neglected.

The model also assumes that all devices in the system contain sufficient energy. In the case of the low frequency devices, this assumption makes it possible to extend the results of the model to multiple devices. The model generates a low frequency power command and assumes that the device can supply it indefinitely. In reality this is not true. Although a generator can be refueled and a battery contains orders of magnitude more energy than an ultracapacitor, they still have energy limits. The model also assumes that the ultracapacitor contains sufficient energy to supply any power required by the high frequency demand. Although the model monitors the energy state of the ultracapacitor, there is nothing that prevents it from being completely depleted.

There is compensation to ensure that it always contains enough energy to supply the high frequency power command; however, the model is based on the assumption that whatever power is commanded, that power can be provided. It is possible to ensure that the controller never requests more power than is available in a simulation where the power profile is known. By generating the high frequency power command before-hand, the profile's high frequency energy requirements can be determined. Based on the energy requirements of the profile and the energy capacity of the ultracapacitor, the corner frequency of the filter can be adjusted to ensure the ultracapacitor is always capable of supplying the commanded power. In the real system, if the devices are not capable of supplying the required power, more energy devices must be added to meet the power demand.

### **System Model Simplification**

The use of these assumptions enables the simplification of the system model. It must be remembered that this process is only for the purpose of the stability analysis, and is not a representation of any physical architecture. These simplifications, though not physically accurate, are mathematically correct. The purpose of this simplification is to provide a simple model which can be easily analyzed and provide an intuitive grasp of the power flow within the system.

The first decision in simplifying the model is to decide how to model the energy sources. The types of devices that are present in the system can be classified as low energy and high energy. The low energy devices, the bus capacitor and the ultracapacitor, can easily be modeled as integrators as shown in the equation below.

$$E(t) = \frac{1}{2} C v(t)^2 = \int (i(t)v(t)) dt \quad 5.2$$

Thus by integrating the net power flowing into the capacitors an energy estimate is obtained. The high energy devices, such as batteries and generators, are much more difficult to model. But since it is assumed that they contain sufficient energy, their modeling is neglected.

Shown below in Figure 5.2 is the dynamic power flow schematic of the simple HyPER system. Note that the energy states of the capacitors are estimated by the power integration. The PI controller generates a power command which is filtered and then sent on to the energy sources. Because of the assumption that the converters transfer the commanded power, the input to the energy source block is identical to the output.

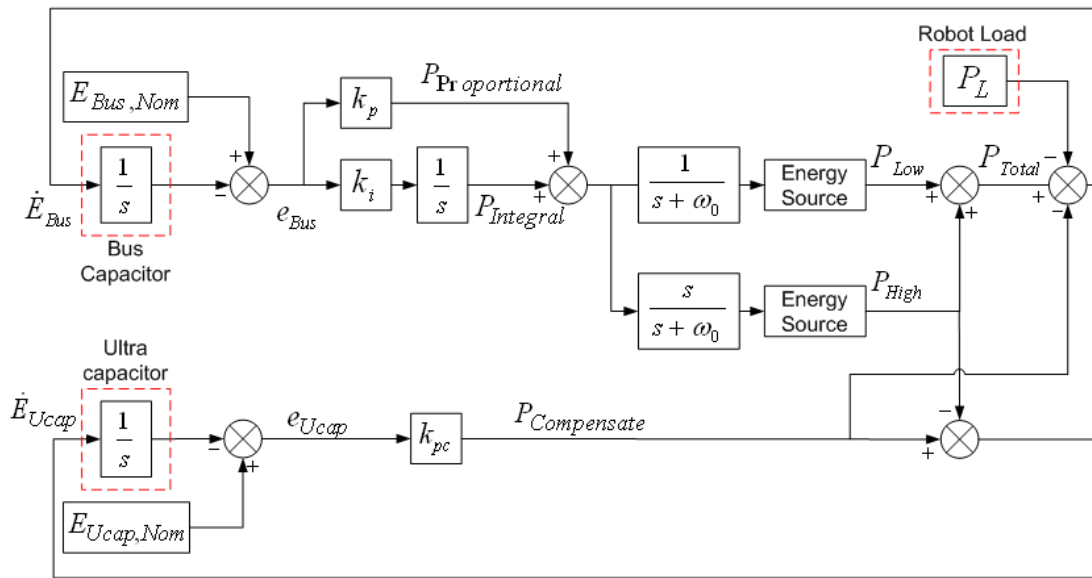


Figure 5.2: HyPER control system representation

This diagram can be further simplified. Since the energy source block input and output are identical, the block will be dropped from the system. Second, the filtering can be simplified. Rather than representing the power flowing onto the bus capacitor from each device as the output of two filters, the output of the PI controller,  $P_{Total}$ , is used. This is possible because the sum of the filter outputs is guaranteed to match the output of the PI controller. This is because of the way that the filter is implemented in the physical system where the output of a low pass filter is

subtracted from the controller output to obtain the high frequency components of the power demand. In Figure 5.2 the controller output is filtered by both a high pass and low pass filter to intuitively demonstrate the power flow of the system. The simplified block diagram is shown in Figure 5.3.

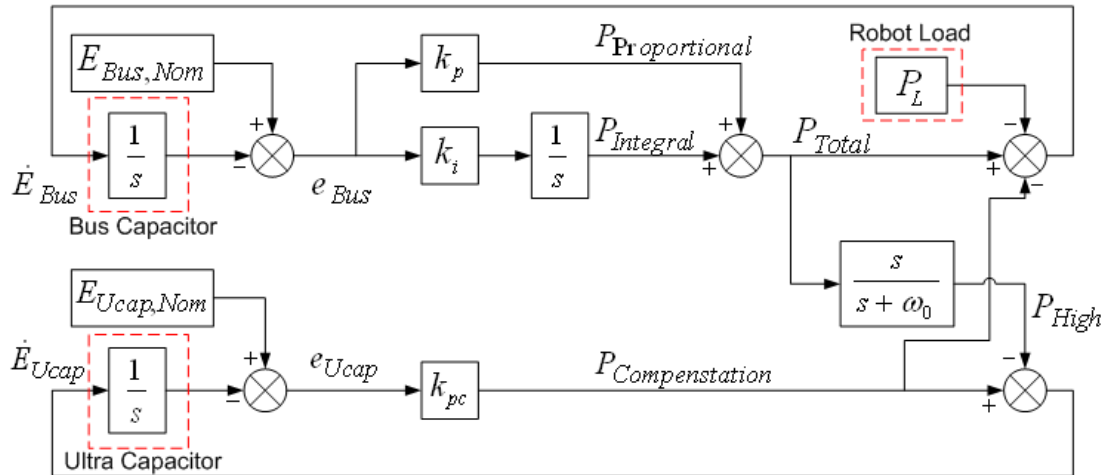


Figure 5.3: Simplified HYPER control system representation

The purpose of this simulation was to build an intuitive model to represent the power flow of the HYPER system. This power flow is regulated by monitoring and regulating the system's energy states. It is easy to lose sight of the physical system in the mathematical model. Therefore, before continuing further with the analysis, the power flow must be verified. In the physical system, there are three power connections to the bus capacitor: the low frequency power connection from the battery, the high frequency power connection from the ultracapacitor, and the main robot power bus. In the model in Figure 5.3 there are four signals which are summed at the input to the bus capacitor. The fourth signal comes from the ultracapacitor recharge draw which in the physical system is on the same connection. The ultracapacitor is supplying the high frequency power demand to the robot power bus, and is also being recharged by the power commanded by the output of the ultracapacitor regulator. Thus, the net power flow into the bus capacitor makes sense intuitively.

### Mathematical Model

In the last section an intuitive energy/power flow model was derived from the HyPER system. It must now be formulated into a mathematical form that can be simulated in the SIMULINK® environment. Starting at the bus capacitor, the net power flowing into the capacitor is

$$P_{Bus} = P_{Total} - P_{Compensation} - P_L \quad 5.3$$

where  $P_{Total}$  represents the power command generated by the PI feedback regulator on the bus energy,  $P_{Compensation}$  represents the power used to recharge the ultracapacitor, and  $P_L$  represents the load demanded by the robot. Following the same procedure, the ultracapacitor net power flow can be derived, which results in the equation 5.4.

$$P_{Ucap} = P_{Compensation} - P_{High} \quad 5.4$$

where  $P_{High}$  is the high frequency power demand from the robot power bus. These two equations are used to form the energy states defined in equation 5.5.

$$\dot{E}_{Bus} = P_{Bus}, \quad \dot{E}_{Ucap} = P_{Ucap} \quad 5.5$$

Two other states are derived from the integral portion of the PI controller,  $P_{Integral}$ , and from the internal state of the high pass filter,  $X$ . The state  $X$  is meaningless, so a change of variable will be performed. The new state,  $P_{Low}$ , represents the low frequency power command, and the variable change is defined in equation 5.6.

$$X = \frac{P_{Low}}{\omega_0} \quad 5.6$$

These four states provide the basis for a state variable description of the LTI HyPER architecture.

$$\begin{aligned} \dot{x}(t) &= Ax(t) + bu(t) \\ y(t) &= Cx(t) + du(t) \end{aligned} \quad 5.7$$

The state vector is defined as

$$x(t) = \begin{bmatrix} E_{Bus} \\ P_{Integral} \\ P_{Low} \\ E_{Ucap} \end{bmatrix} \quad 5.8$$

where  $E_{Bus}$  is the energy stored in the bus capacitor,  $P_{Integral}$  is the integral term output of the PI controller,  $P_{Low}$  is the state internal to a state space model of the filter and the low frequency power command, and finally  $E_{Ucap}$  is the energy stored in the ultracapacitor. By writing the loop equations describing Figure 5.3, the state space equations for the state vector can be derived. The first state,  $E_{Bus}$ , is a function of three power terms. Two of these power terms are derived in equations 5.9-5.10.

$$\begin{aligned} P_{Compensation} &= k_{pc}e_{Ucap} \\ &= k_{pc}(E_{Ucap,Nom} - E_{Ucap}) \\ &= k_{pc}E_{Ucap,Nom} - k_{pc}E_{Ucap} \end{aligned} \quad 5.9$$

$$\begin{aligned}
P_{Total} &= P_{Integral} + P_{Proportional} \\
&= P_{Integral} + k_p e_{Bus} \\
&= P_{Integral} + k_p (E_{Bus,Nom} - E_{Bus}) \\
&= P_{Integral} + k_p E_{Bus,Nom} - k_p E_{Bus}
\end{aligned} \tag{5.10}$$

The third power term contributing to the bus energy is  $P_L$ , which is the load demanded by the robot. By substituting these equations into equation 5.3, the state equation for  $E_{Bus}$ , shown in equation 5.11, is complete.

$$\begin{aligned}
\dot{E}_{Bus} &= -P_{Compensation} + P_{Total} - P_L \\
&= -(k_{pc} E_{Ucap,Nom} - k_{pc} E_{Ucap}) + P_{Total} - P_L \\
&= -k_{pc} E_{Ucap,Nom} + k_{pc} E_{Ucap} + P_{Total} - P_L \\
&= -k_{pc} E_{Ucap,Nom} + k_{pc} E_{Ucap} + P_{Integral} + k_p E_{Bus,Nom} - k_p E_{Bus} - P_L
\end{aligned} \tag{5.11}$$

The second state,  $P_{Integral}$  only has one input term, the bus energy error,  $e_{Bus}$ . This error term is reduced to its original components in equation 5.12,

$$\begin{aligned}
\dot{P}_{Integral} &= k_i e_{Bus} \\
&= k_i (E_{Bus,Nom} - E_{Bus}) \\
&= -k_i E_{Bus} + k_i E_{Bus,Nom}
\end{aligned} \tag{5.12}$$

where  $E_{Bus,Nom}$  is the bus energy setpoint. The internal state of the filter is defined in equation 5.13.

$$\dot{X} = -\omega_0 X + P_{Total} \tag{5.13}$$

As discussed previously, the change of variable will be performed resulting in equation 5.14.

$$\begin{aligned}
\dot{P}_{Low} &= -\omega_0 P_{Low} + \omega_0 P_{Total} \\
&= -\omega_0 P_{Low} + \omega_0 (P_{Integral} - k_p E_{Bus,Nom} + k_p E_{Bus})
\end{aligned}
\tag{5.14}$$

The output of the filter,  $P_{High}$  or the high frequency power command is shown in equation 5.15.

$$P_{High} = -P_{Low} + P_{Total} \tag{5.15}$$

Substituting the two power input equations into equation 5.4, the state equation is defined in terms of only the system inputs and other states.

$$\begin{aligned}
\dot{E}_{Ucap} &= -P_{High} + P_{Compensation} \\
&= -P_{High} + k_{pc} E_{Ucap,Nom} - k_{pc} E_{Ucap} \\
&= -(-P_{Low} + P_{Integral} - k_p E_{Bus,Nom} + k_p E_{Bus}) + k_{pc} E_{Ucap,Nom} - k_{pc} E_{Ucap} \\
&= P_{Low} - P_{Integral} + k_p E_{Bus,Nom} - k_p E_{Bus} + k_{pc} E_{Ucap,Nom} - k_{pc} E_{Ucap}
\end{aligned}
\tag{5.16}$$

The state equations are now all defined and are summarized in equation 5.17.

$$\begin{aligned}
\dot{E}_{Bus} &= -k_p E_{Bus} + P_{Integral} + k_{pc} E_{Ucap} + k_p E_{Bus,Nom} - k_{pc} E_{Ucap,Nom} - P_L \\
\dot{P}_{Integral} &= -k_i E_{Bus} + k_i E_{Bus,Nom} \\
\dot{P}_{Low} &= \omega_0 k_p E_{Bus} + \omega_0 P_{Integral} - \omega_0 P_{Low} - \omega_0 k_p E_{Bus,Nom} \\
\dot{E}_{Ucap} &= -k_p E_{Bus} - P_{Integral} + P_{Low} - k_{pc} E_{Ucap} + k_p E_{Bus,Nom} + k_{pc} E_{Ucap,Nom}
\end{aligned}
\tag{5.17}$$

These equations must now be rearranged to fit the form of the state space matrix equations shown in equation 5.7. The final matrix expression of the system equations is shown in equation 5.18.

$$\begin{bmatrix} \dot{E}_{Bus} \\ \dot{P}_{Integral} \\ \dot{P}_{Low} \\ \dot{E}_{Ucap} \end{bmatrix} = \begin{bmatrix} -k_p & 1 & 0 & k_{pc} \\ -k_i & 0 & 0 & 0 \\ \omega_0 k_p & \omega_0 & -\omega_0 & 0 \\ -k_p & -1 & 1 & -k_{pc} \end{bmatrix} \begin{bmatrix} E_B \\ P_{Integral} \\ P_{Low} \\ E_{Ucap} \end{bmatrix} + \begin{bmatrix} k_p \\ k_i \\ -\omega_0 k_p \\ k_p \end{bmatrix} E_{Bus,Nom} + \begin{bmatrix} -k_{pc} \\ 0 \\ 0 \\ k_{pc} \end{bmatrix} E_{Ucap,Nom} - \begin{bmatrix} P_L \\ 0 \\ 0 \\ 0 \end{bmatrix} \quad 5.18$$

The inputs  $E_{Bus,Nom}$  and  $E_{Ucap,Nom}$  are not dynamic inputs, but rather the setpoints for the bus capacitor energy and ultracapacitor energy, respectively.

### Model Simulation

Before continuing with the analysis, the system should be simulated to ensure that the results of the control system simulation agree with the results of the full system simulation covered in Chapter 4. Shown in Figure 5.4 is the SIMULINK® block diagram representing the control analysis system.

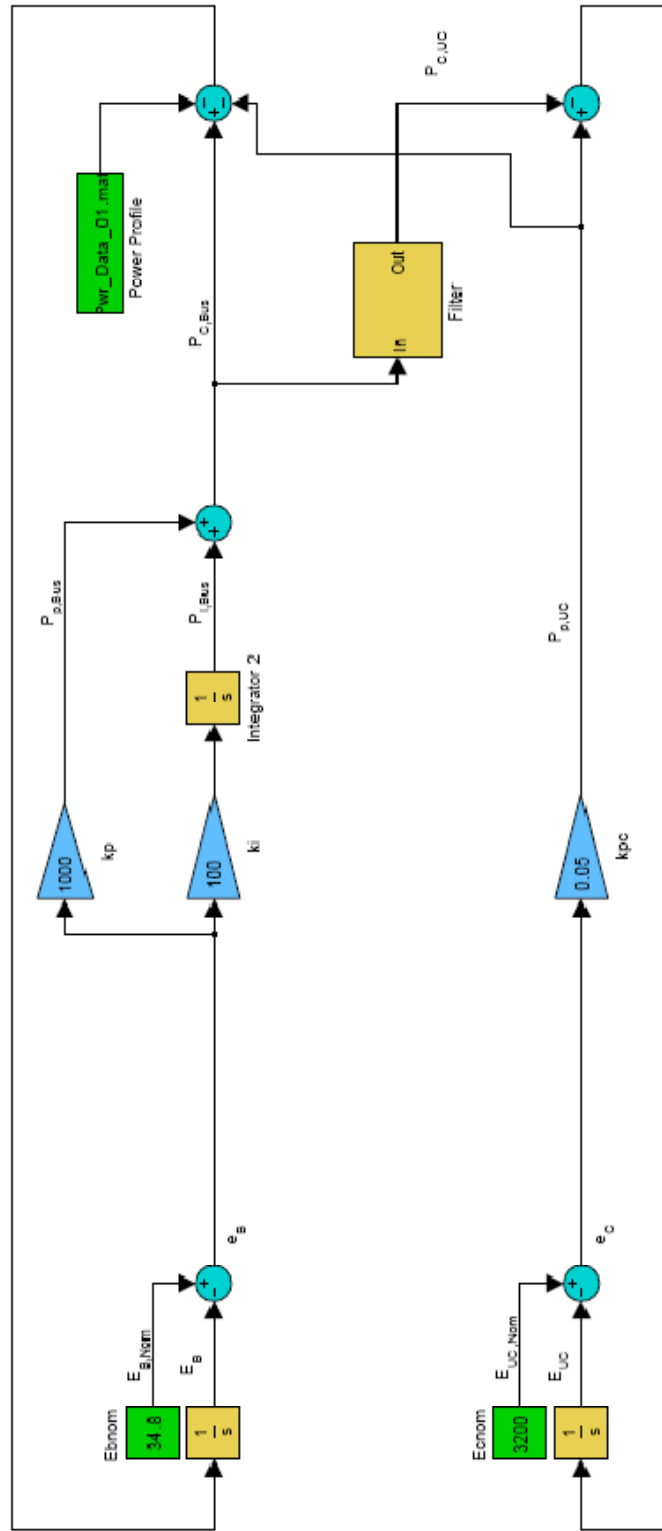


Figure 5.4: SIMULINK® control system simulation

First the simulation will be run with  $k_{pc} = 0$  which is the same as running without the ultracapacitor recharge circuit. It can be seen from the results in Figure 5.5 that the controller properly regulates the energy states of the bus capacitor and the ultracapacitor. One major difference between the simulation and the physical system is that the ultracapacitor energy does not decrease significantly over the course of the cycle in the simulation.

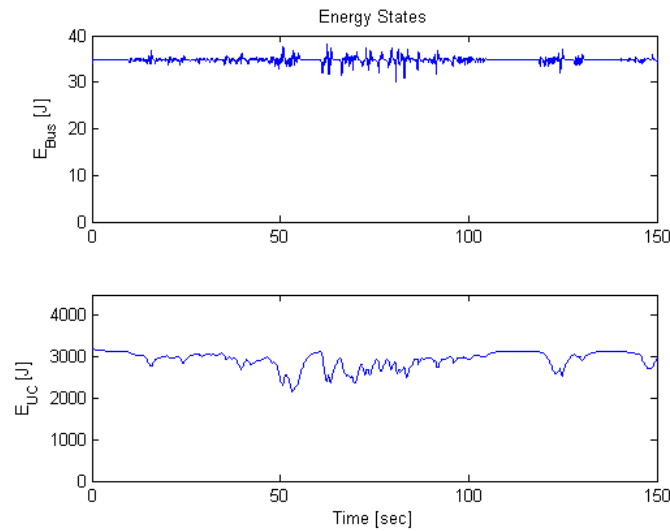


Figure 5.5: Simulation energy states,  $k_{pc} = 0$

The ultracapacitor charging gain was changed to  $k_{pc} = 0.05$ , and the ultracapacitor energy does not decrease at all. One of the assumptions this control model is based on is that the converter losses can be thought of as a disturbance. In this model the disturbance is artificially set to zero, and thus there is essentially no net loss of energy in the ultracapacitor.

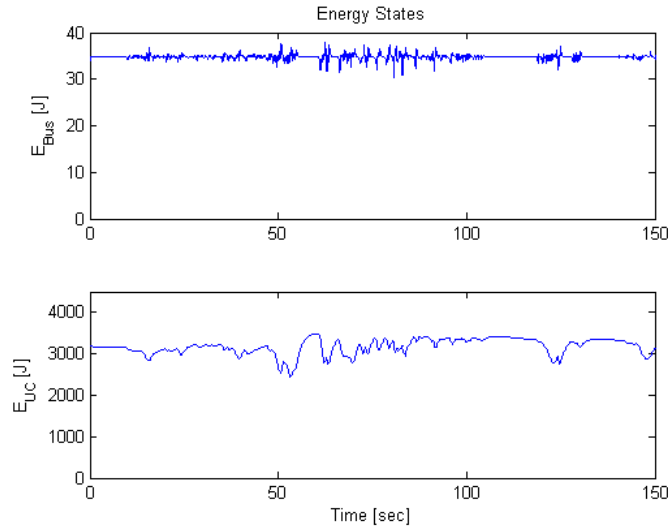


Figure 5.6: Simulation energy states,  $k_{pc} = 0.05$

These results are sufficiently close to the full system simulation to verify that the control analysis simulation is a close approximation of the actual system. The disturbance in the system will actually tend to make the system more stable. In order to show that the system is stable it must be shown that the  $Re\{eig(A)\} < 0$ . This could be done analytically, but is shown here using a root locus method. There are four different variables which can be used to tune the performance of the state space in equation 5.19.

$$\begin{bmatrix} \dot{E}_{Bus} \\ \dot{P}_{Integral} \\ \dot{P}_{Low} \\ \dot{E}_{Ucap} \end{bmatrix} = \begin{bmatrix} -k_p & 1 & 0 & k_{pc} \\ -k_i & 0 & 0 & 0 \\ \omega_0 k_p & \omega_0 & -\omega_0 & 0 \\ -k_p & -1 & 1 & -k_{pc} \end{bmatrix} \begin{bmatrix} E_B \\ P_{Integral} \\ P_{Low} \\ E_{Ucap} \end{bmatrix} + \begin{bmatrix} k_p \\ k_i \\ -\omega_0 k_p \\ k_p \end{bmatrix} E_{Bus,Nom} + \begin{bmatrix} -k_{pc} \\ 0 \\ 0 \\ k_{pc} \end{bmatrix} E_{Ucap,Nom} - \begin{bmatrix} P_L \\ 0 \\ 0 \\ 0 \end{bmatrix} \quad 5.19$$

These variables are  $k_i$ , the integral gain,  $k_p$ , the proportional gain,  $k_{pc}$ , the proportional ultracapacitor recharge gain, and  $\omega_0$ , the filter corner frequency. The first three are the variables of interest. The placement of  $\omega_0$  mostly affects the sizing of the ultracapacitor. Shown in Figure 5.7 are the system pole locations while the integral gain,  $k_i$ , is varied from 5 to 1000.

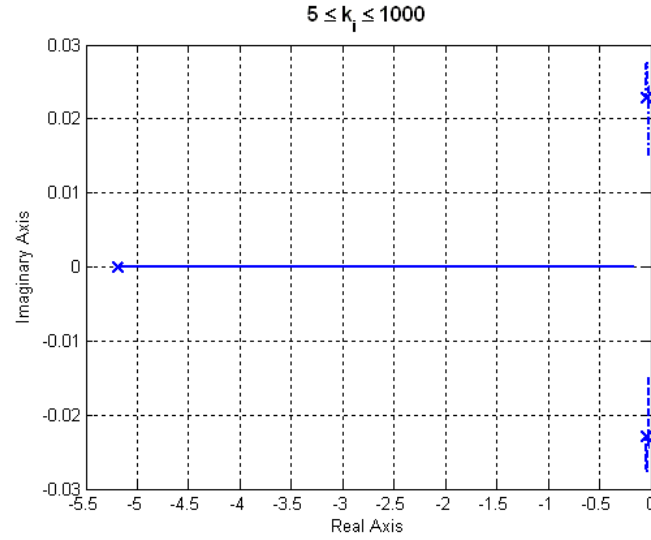


Figure 5.7: System root loci,  $5 \leq k_i \leq 1000$

Figure 5.7 shows that the system is stable as all  $Re\{eig(A)\} < 0$ . Figures 5.8 - 5.11 show the movement of the system pole locations as the different gains in equation 5.19 are varied.

There is a circle placed at the final pole location when the gain has reached its maximum value.

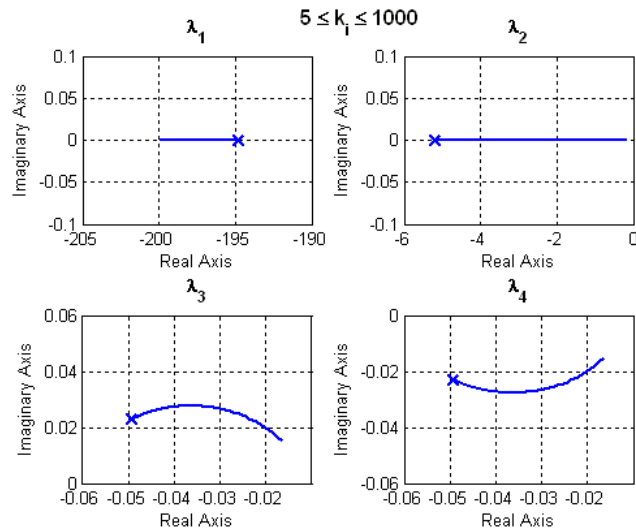
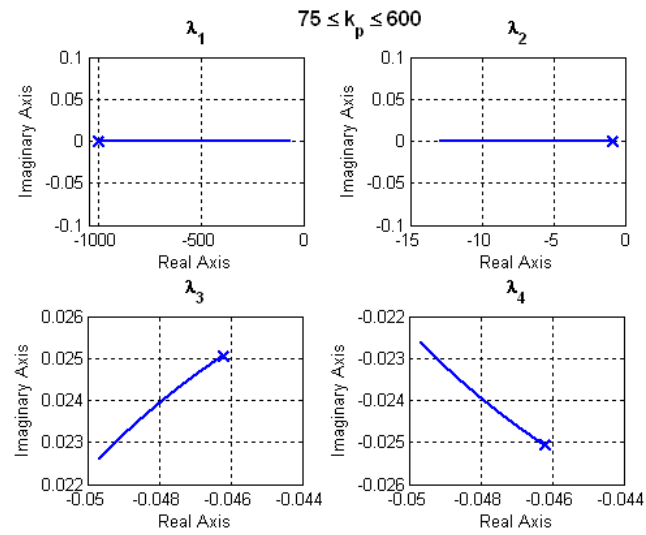
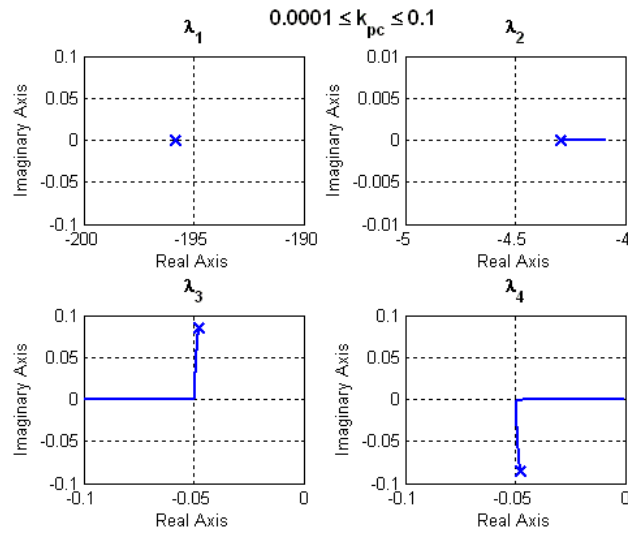


Figure 5.8: System root loci,  $5 \leq k_i \leq 1000$

Figure 5.9: System root loci,  $75 \leq k_p \leq 600$ Figure 5.10: System root loci,  $0.0001 \leq k_{pc} \leq 0.1$

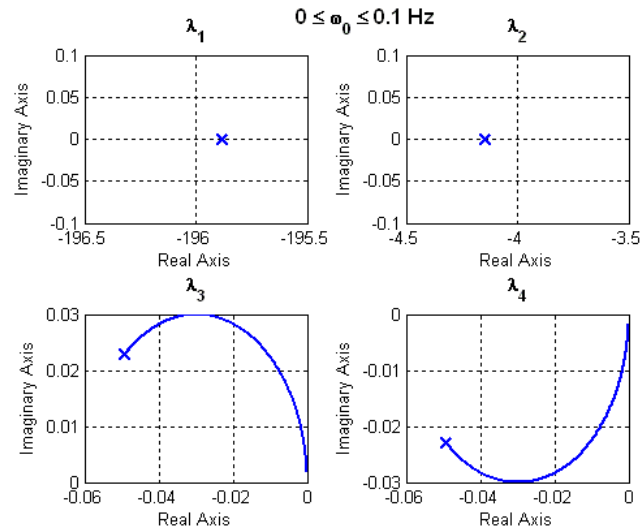


Figure 5.11: System root loci,  $0 \leq \omega_0 \leq 0.1$

The root locus analysis shows that the HyPER system is stable when the controller gains are properly set. The setpoints for the gains during the various tests are recorded in Table 5.1. Although the system is stable, the poles showed some interesting behavior at times. Figure 5.8-5.9 show the affect the gains  $k_i$  and  $k_p$  have on the poles  $\lambda_1$  and  $\lambda_2$ . As the gains approach zero one of the poles in each figure approaches the imaginary axis and marginal stability. This also occurs in Figure 5.10 as the gain,  $k_{pc}$ , approaches zero. Marginal stability causes the state to be completely dependent on the input. In the case of  $k_i$  and  $k_p$  marginal stability causes the states to be solely dependent the robot power demand which would quickly drive the states to zero. In the case of  $k_{pc}$  marginal stability causes the state to be dependent on the high frequency power demand and the disturbance. Since the disturbance is guaranteed to only draw power from the ultracapacitor, the state is driven to zero or, in other words, the ultracapacitor is completely depleted.

	$k_i$	$k_p$	$k_{pc}$	$\omega_0$
$k_i$		800	800	800
$k_p$	200		200	200
$k_{pc}$	0.05	0.05		0.05
$\omega_0$	0.1	0.1	0.1	

Table 5.1: Controller setpoints

### Summary

It was found that the controlled HyPER system could be simplified to enable the use of linear control theory. The simplifications were based on certain assumptions which can be made about the system and its operation. The simplified model was verified through a simulation, and the results from the simulation were sufficiently close to the results of the simulation of the full HyPER system. After being verified, the state space model of the system was derived. Using a state space model, it was shown that the eigenvalues of the system all lay in the left half of the complex plane. The use of root locus plots shows that the system is stable over a wide range of gain values.

## **Chapter 6**

### **Converter Testing**

The design of the bidirectional converter was discussed in Chapter 2, and the data acquired through the hardware testing was used in the development of a system model. In this chapter the test bench and the testing of the converter are described. This testing is conducted over a wide range of operating conditions, and the converter operating setpoints are also changed to find the optimal setpoints for its operation. The results of this testing are shown, and efficiency curves for the converter operation are generated. Finally, the losses in the converter are analyzed and separated into their component parts.

#### **Test Setup**

The purpose of this experiment is not to test how well the converter works with any particular source or load, but to test the efficiency of the conversion. Thus the source that is used is a 900 W power supply. This supply will not completely test the range of the converter, but it is the largest variable voltage power supply available. The sink is a set of three 12 volt batteries connected in series to form a 36 volt bus. This bus is in parallel with a load bank which is set at a constant voltage limit of 36 volts. This ensures that the bus voltage is forced to be constant and the test is performed in a controlled environment.

The procedure to test the converters is to run the converter at 25% load for approximately five minutes before the actual test begins. This warms all the components so that false readings are not obtained due to the low resistance of cold traces. Then the command current, starting at zero, is incremented, and both the input and output voltage and current data are recorded. This

step is repeated until the command current is equal to thirty amps. Near zero, where the converter is the least efficient, the increments are small. As the current increases the step size increases. A total of twelve different tests were run. Three different input voltages; 15, 24, and 33; were used. These three input voltage tests were also run at four different switching frequencies (49.5 kHz, 58.3 kHz, 71.5 kHz, and 92.6 kHz).

### Testing Results

The next three plots Figures 6.1-6.3 show the operating set points of the converter during the tests. Figure 6.1 shows the operation with an input voltage at approximately 15 volts. On the x-axis is shown the sample numbers. As previously noted it can be seen in the second and third subplots of each figure that the step size was kept relatively small. This ensures that the efficiency curves completely map the operation of the converters.

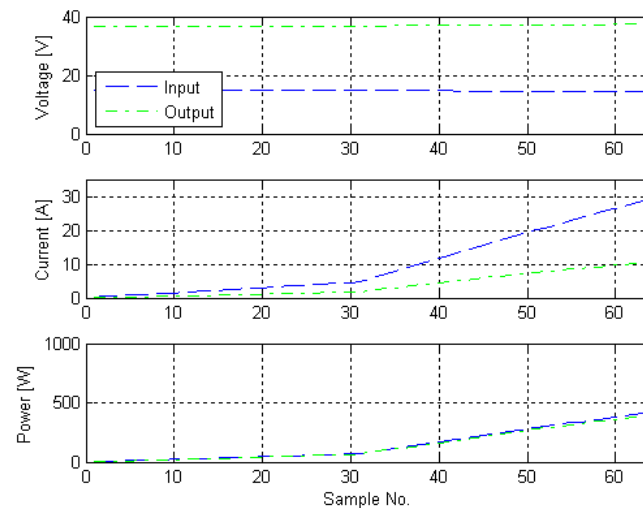


Figure 6.1: Converter testing variables,  $V_{in} = 15$

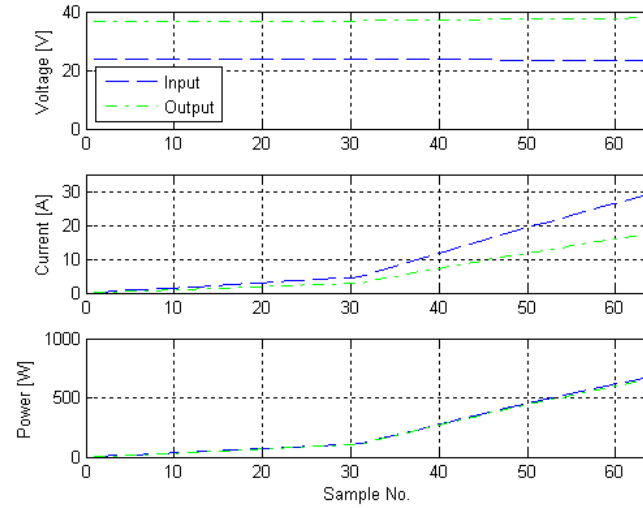


Figure 6.2: Converter testing variables,  $V_{in} = 24$

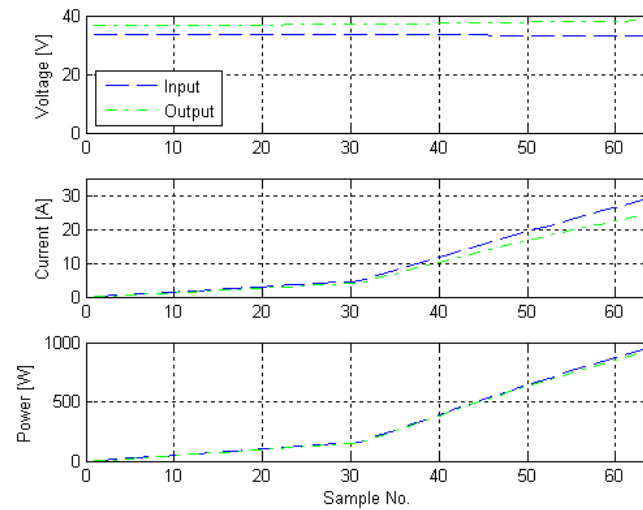


Figure 6.3: Converter testing variables,  $V_{in} = 33$

It should be noted that each figure represents the average operating conditions from twelve different tests. At each switching frequency set point the test was conducted three times to ensure that no particular test was an outlier. At the conclusion of each test it was noted that the tests were all practically indistinguishable from an input-output point of view.

In Figures 6.4-6.6 the efficiency curves of each test are shown. It should be noted that the efficiency plots demonstrate the differences between each test which are not readily apparent in the input-output figures previously shown. Each plot line represents the average of three tests at a voltage set point.

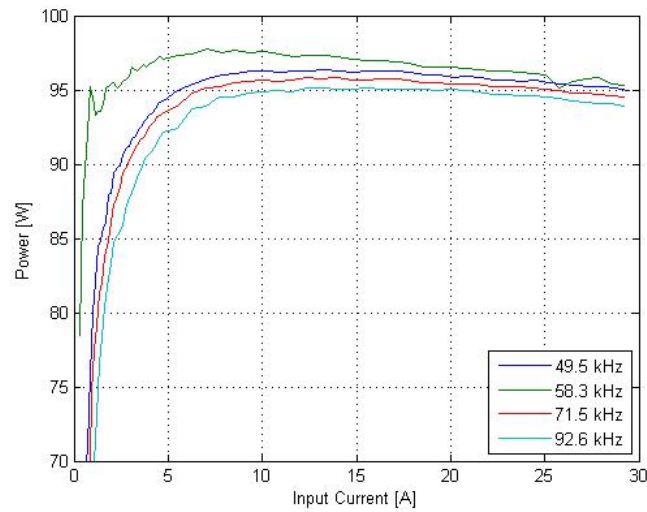


Figure 6.4: Converter efficiency,  $V_{in} = 15$

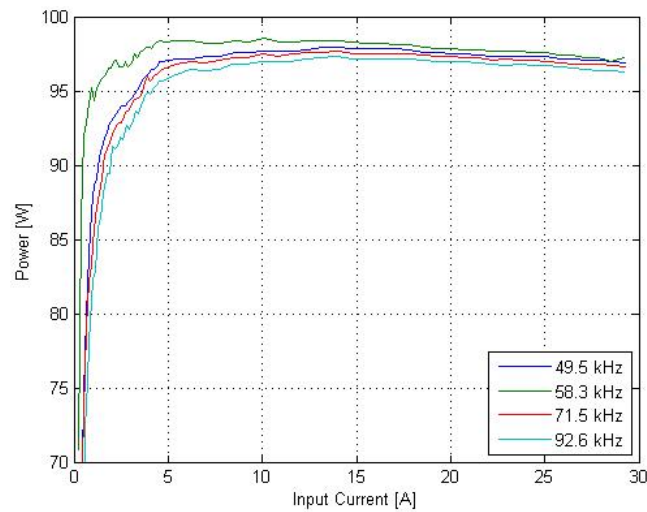


Figure 6.5: Converter efficiency,  $V_{in} = 24$

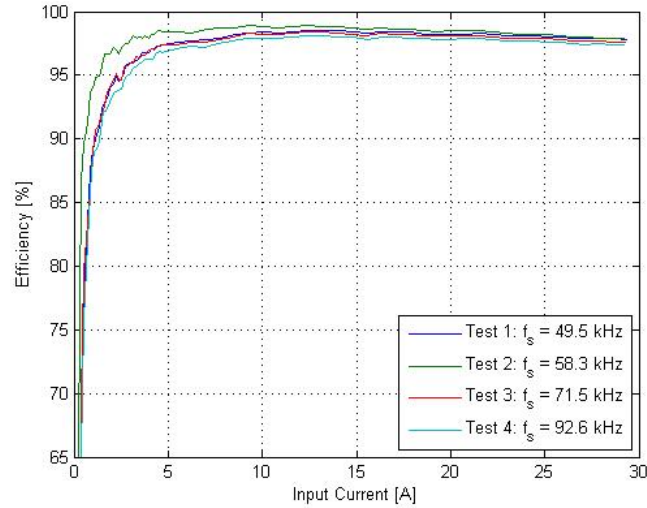


Figure 6.6: Converter efficiency,  $V_{in} = 33$

As expected, tests in which the switching frequency was high, 92.6 kHz, the switching losses negatively impacted the efficiency of the converter. However, the most efficient operating point is not the lowest, but rather the second from the lowest, 58.3 kHz. At this point some other inefficiency is becoming more prominent. Interestingly, the highest efficiency is significantly more efficient than the other curves in the plot, especially at low input voltages. If this occurred in just one test it would indicate a testing error had occurred. However, since it occurred in all twelve tests, it indicates that it is indeed a valid operating point. Several factors could account for the significant efficiency increase. The inductor is oversized for the converter. This allows a lower switching frequency while achieving the output ripple current requirements. The switching frequency can only be decreased so far before the converter enters discontinuous conduction mode (DCM) which decreases the efficiency of the conversion process. However, the boundary between continuous and discontinuous conduction modes, known as boundary conduction mode (BCM), provides a highly efficient operating point. When operating at BCM, there is no current through the MOSFETs during the switching cycle. This effectively makes the switching losses zero and could explain the significant efficiency increase of the converter.

The previous plots compare the efficiency of the converter at different operating conditions. However, it only tells half the story. Using current as the x-axis does not demonstrate the effect that the input voltage has on efficiency vs. power. Figures 6.7-6.9 show the efficiency versus power support this point.

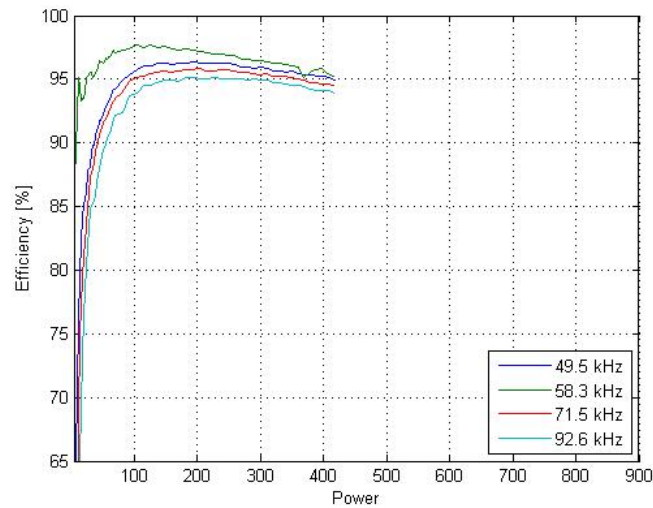


Figure 6.7: Converter efficiency vs. power,  $V_{in} = 15$

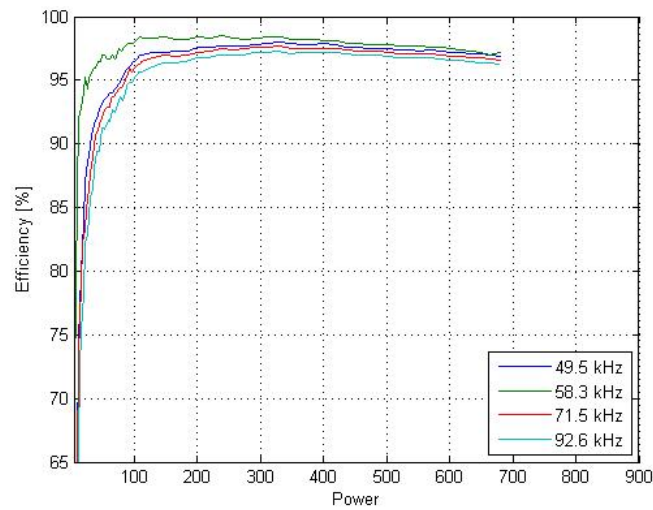


Figure 6.8: Converter efficiency vs. power,  $V_{in} = 24$

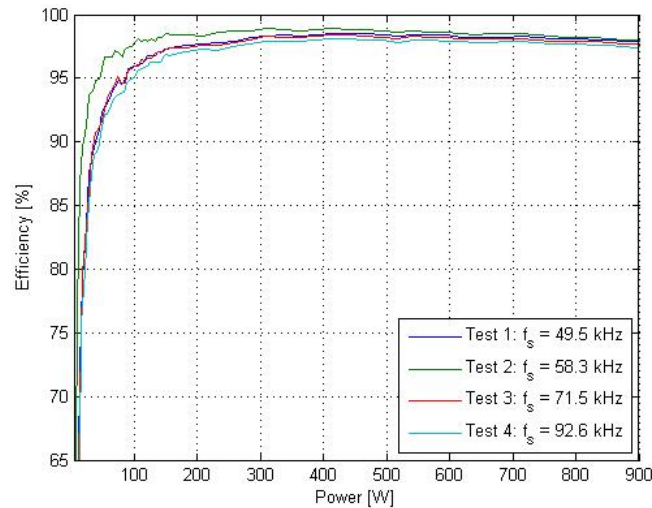


Figure 6.9: Converter efficiency vs. power,  $V_{in} = 33$

From these figures the effect of the input voltage on the efficiency and maximum power transfer is easily seen. In order to transfer power efficiently over the entire range, the input voltage should be close to the output voltage. The efficiency of the overall system is based on the operating efficiency of the individual converters. For the overall efficiency to be good, assume over 90%, the converters must be operating, on average, above 90%. Using the efficiency curves as a guide, the power allocations can be refined to optimize the system efficiency.

Now that the efficiency of the converters has been shown, what are its loss mechanisms? The converter's estimated losses were presented in Chapter 2, and the loss mechanisms used in that estimation are now described more in depth. Figure 6.10 shows the analytical breakdown of the losses in the converter, which were explained in equations 6.1-6.2. The original estimated loss mechanism values are now adapted to fit the loss breakdown to the empirical efficiency curves.

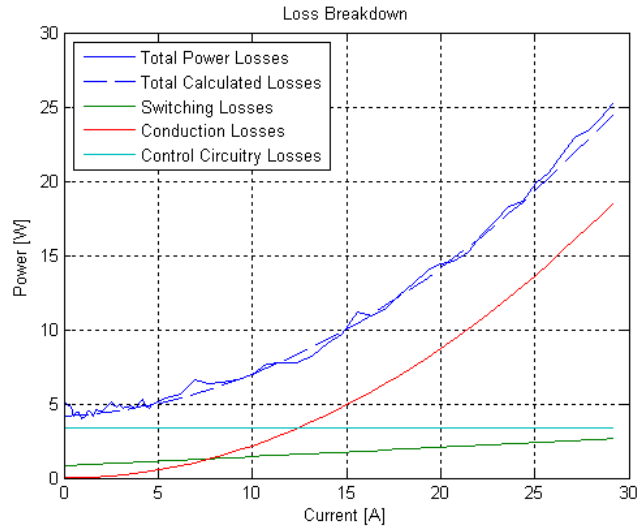


Figure 6.10: Converter loss breakdown

The conduction losses are the single largest loss mechanism and can be described by the following equation. For all calculations the duty cycle,  $D$ , was calculated by dividing the input voltage by the output voltage.

$$P_{conduction} = R_{ds,on}(I_{out}^2(1 - D) + I_{in}^2 D) + R_{winding}I_{in}^2 + R_s I_{in}^2 + V_{dss}I_{dss} \quad 6.1$$

The various conduction losses in the converter are due to the MOSFET on state resistance,  $R_{ds,on}$ , the PCB trace and inductor winding losses,  $R_{winding}$ , and the sense resistor loss,  $R_s$ . The last loss mechanism which is lumped in with the conduction, although it is a property of the MOSFETs is the drain to source leakage power,  $V_{dss}I_{dss}$ . This obviously is not an in depth model of the conduction losses, however it is sufficient for the modeling that is necessary for the project. There are also AC conduction losses in the inductor due to skin effect within the inductor windings.

The next largest losses are the DC losses from the control circuitry, drive circuitry, and the isolated power supplies. At low operating powers, this loss has the most significant impact on the converter efficiency, and thus must be minimized in any future converter designs.

The MOSFET switching losses are the least significant, and are proportional to the current through the MOSFETs. The losses are described by equation 6.2.

$$P_{switch} = \frac{1}{2}V_{out}I_{out}f_s t_{switch} + \frac{1}{2}V_{out}I_{in}f_s t_{switch} \quad 6.2$$

Where the  $t_{switch}$  represents the time it takes for the MOSFET change from open to closed or closed to open, and  $f_s$  represents the switching frequency of the converter.

### Summary

This chapter covered the testing of the bidirectional converter, and the test conditions described. The input voltage and current as well as the output voltage and current were monitored to allow the calculation of the input-output efficiency. The converter was tested at three different input voltages, and at each voltage the entire range of current was tested. The switching frequency of the converter was tested at four different setpoints, and it was found that the converter operated most efficiently at 58 kHz. The data was plotted versus input current and was also plotted versus the input power to demonstrate the effects of the input voltage on conversion efficiency. It was found that the efficiency of the converter peaks at approximately 98% and except at the lowest operating setpoints, the converter is operating at over 95% efficiency. Finally, an analysis of the converter losses was conducted.

## **Chapter 7**

### **HyPER System Testing**

After system simulation, control algorithm analysis, and component testing, the components can be integrated to form the hybrid power and energy architecture. This chapter discusses the construction of a test bench to simulate the on-platform operation of the system. The supervisory controller is implemented on a real-time controller which allows data logging and allows the operator to change any parameter in the control system. The system is subjected to a real world robot power load generated by an electronic load bank. The performance of the system under load and the results of the testing are shown.

#### **HyPER Test Platform**

Before integrating the system on an actual robotic platform, a fully instrumented test bench, shown in Figure 7.1, was built. To be a good representation of a real robot, the bench has to be able to load the system with a power demand identical to the robot's power demand. To simulate this load, the robot power profile used in the system simulation is implemented using a load bank. The load bank is operated in a current mode. When operated in this mode the load bank will sink a commanded current regardless of the voltage. This allows the HyPER power system to set and regulate the output voltage. The test bench was built with the capability to integrate an ultracapacitor, batteries, and a generator. Though the test bench is capable of demonstrating the use of all three devices simultaneously, only the ultracapacitor and battery are used in order to be consistent with the analysis in previous chapters.

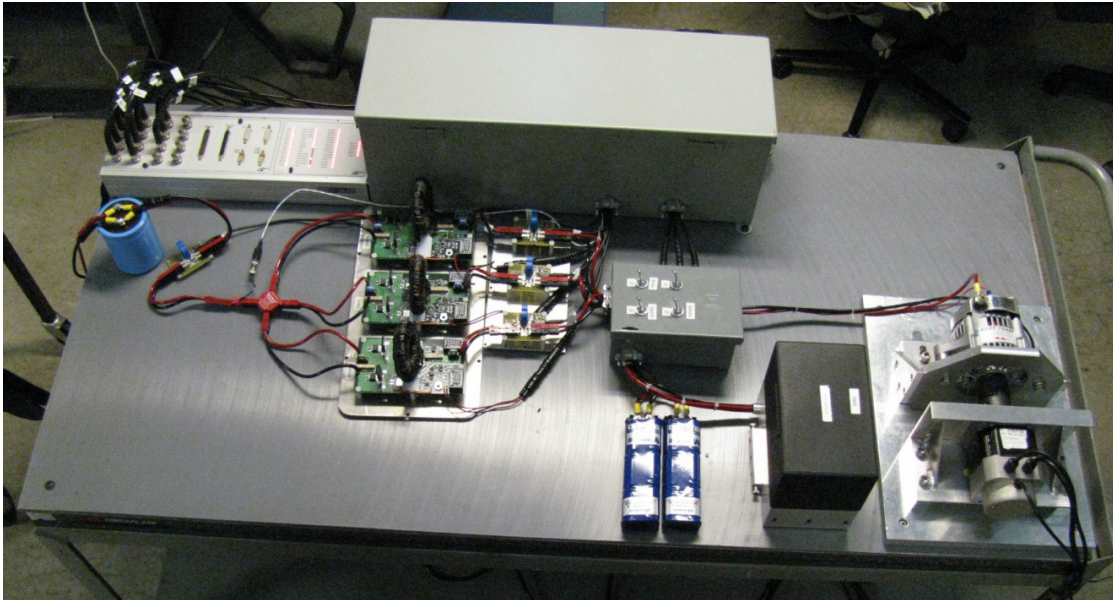


Figure 7.1: HyPER test bench

The three bidirectional DC-DC converters are the core of the bench as they interface the devices to the power bus. The ultracapacitor is made up of two Maxwell Boostcaps, which when combined create a 10 farad, 30 volt ultracapacitor with a peak storage capability of 4300 joules. The low frequency device is a Brentronics BB2590 LiIon battery which, in a series configuration, is nominally a 28 volt battery. Also shown in the lower right of Figure 7.1 is the generator. It has been used successfully in the system to either replace the batteries or to insert a third energy device. The bus capacitor is a standard electrolytic capacitor. The final portion of the HyPER system is the supervisory controller. This has not yet been implemented as an embedded solution, and is currently implemented on dSpace, a real time control system.

The test bench is fully instrumented. There is a current sensor associated with each device including the bus capacitor, and the voltage of each device is measured. Between each converter and its respective device is a switch to enable the quick shutdown of the system in case of emergency. The large gray box is the interface between the system and the dSpace hardware.

The dSpace system also provides the operator with real time data acquisition and control of the system through a user interface which can be seen in the following figure.

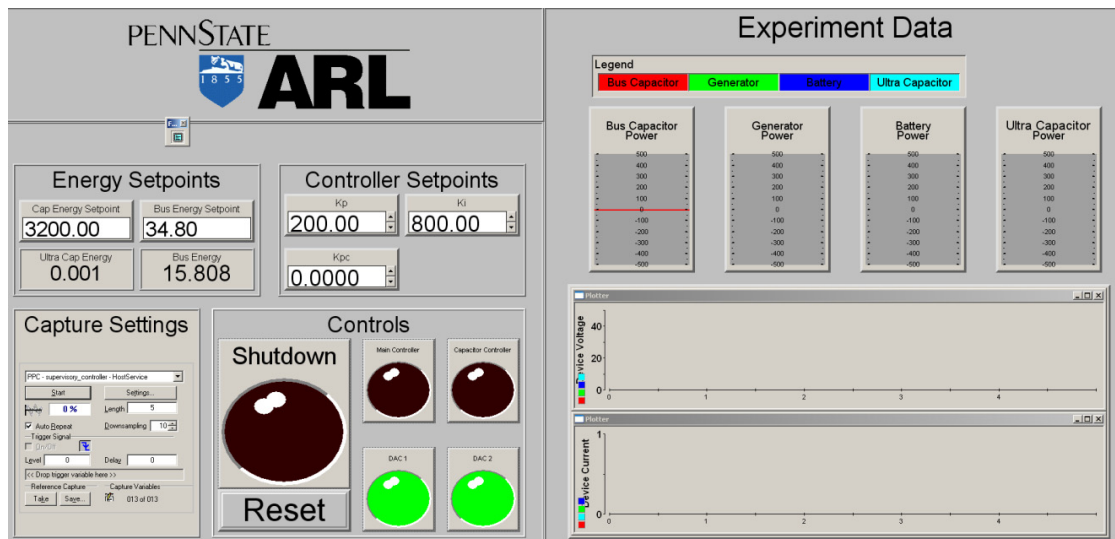


Figure 7.2: dSpace HyPER GUI

This user interface provides the means to access any variable within the controller implemented in the SIMULINK® model shown in Figure 7.3.

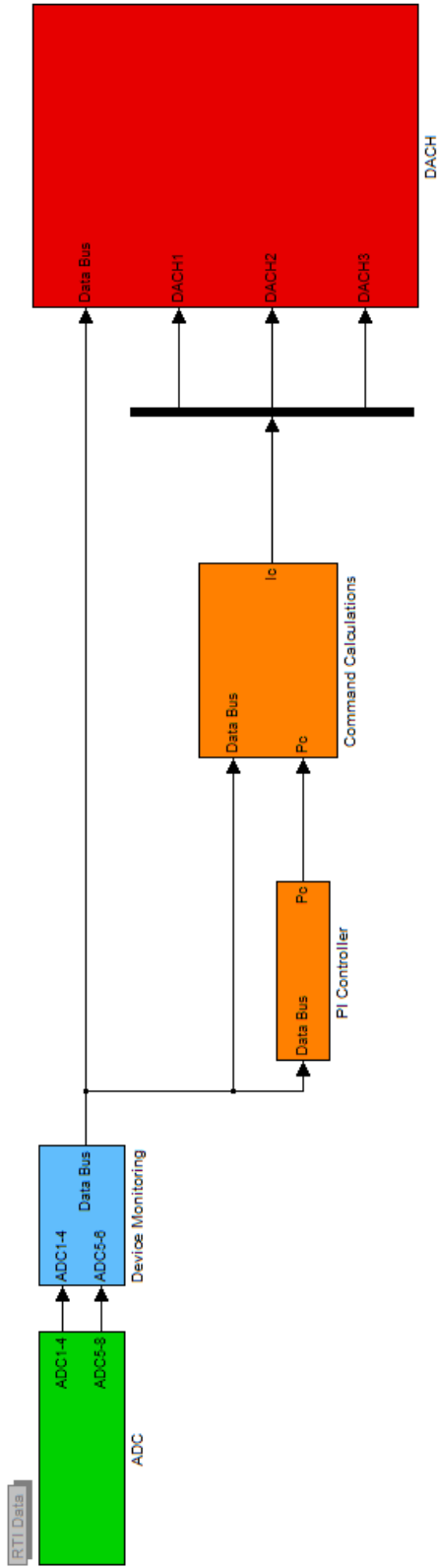


Figure 7.3: dSpace SIMULINK® control model

## Testing

As mentioned previously, the same robot power profile is be used in the system hardware testing as was used in the simulations in previous chapters, and is shown in Figure 7.4.

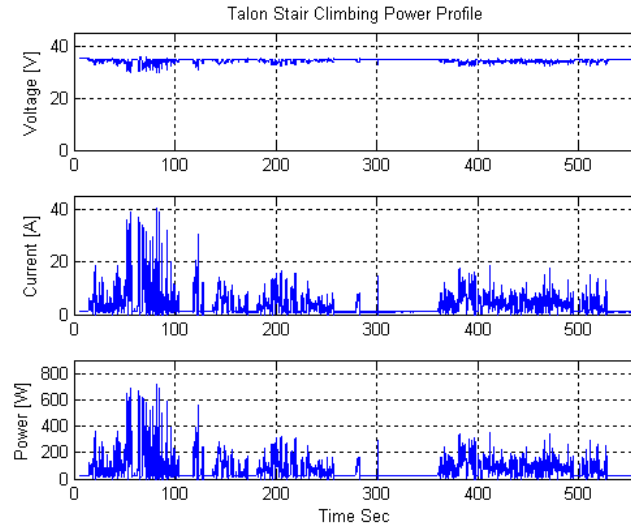


Figure 7.4: Talon® stair climbing power profile

This profile is applied through the electronic load bank to simulate the robot power demand.

Shown below in Table 7.1 are the control parameter settings for the experimental setup on five different runs.

	$k_p$	$k_i$	$k_{pc}$	$\omega_0$
Run 1	200	800	0	0.1
Run 2	200	800	0.001	0.1
Run 3	200	800	0.005	0.1
Run 4	200	800	0.01	0.1
Run 5	200	800	0.05	0.1

Table 7.1: Supervisory controller set points

Before showing the full results of the experiment, the ultracapacitor energy will be compared for all the runs in Figure 7.5. As expected in Run 1, with  $k_{pc} = 0$ , the ultracapacitor's stored energy decays relatively quickly. Thus in subsequent experimental runs, the proportional gain,  $k_{pc}$ , was varied between 0.001 and 0.05.

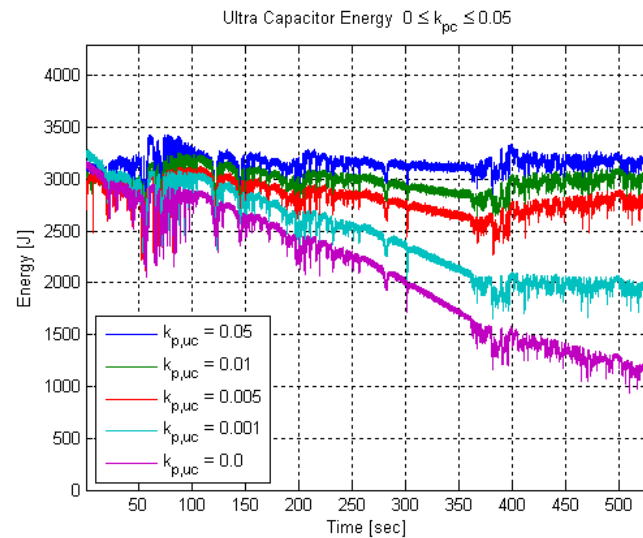


Figure 7.5: Ultracapacitor energy for various  $k_{pc}$  values

This feedback term has a significant effect on the energy stored in the ultracapacitor. From Figure 7.5 it can be seen that  $k_{pc} = 0.05$  is probably too tight a control, as the ultracapacitor is not utilized to its full potential. In the rest of the figures which demonstrate the system's performance, the controller settings for Run 3 will be used and can be found in Table 7.1.

Figure 7.6 demonstrates that the controller for the system functions as desired and stabilizes the bus capacitor energy. The first subplot shows the energy of the bus capacitor. For most of the run the maximum error is less than two joules. The second subplot shows that the ultracapacitor maintains its energy over the course of the entire profile.

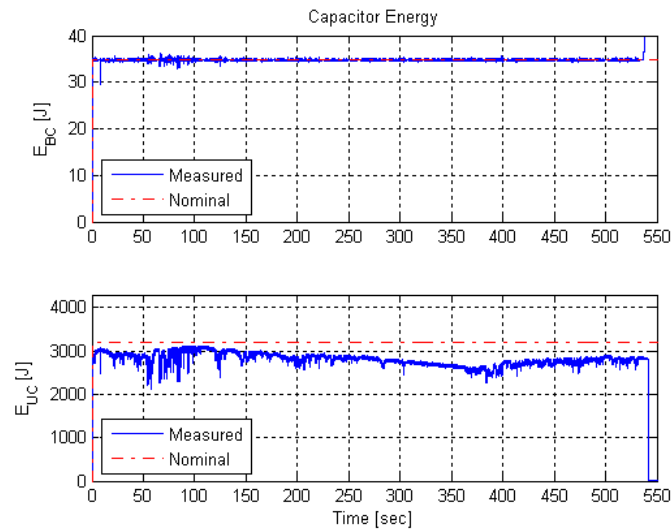


Figure 7.6: Capacitor levels

Figure 7.7 shows the battery variables for the entire run. From the top subplot it can be seen that the assumption made in the system model was justified. The voltage of the battery is relatively constant. It varies slightly under high current draws, but never drops more than two volts for a short period of time. The second subplot shows the current draw, and the bottom subplot shows the power draw. The filtering algorithm works properly, as the battery is only loaded with the low frequency power demand. The plot shows that there is measurement noise present in the system, a very high frequency noise superimposed on the low frequency power demand.

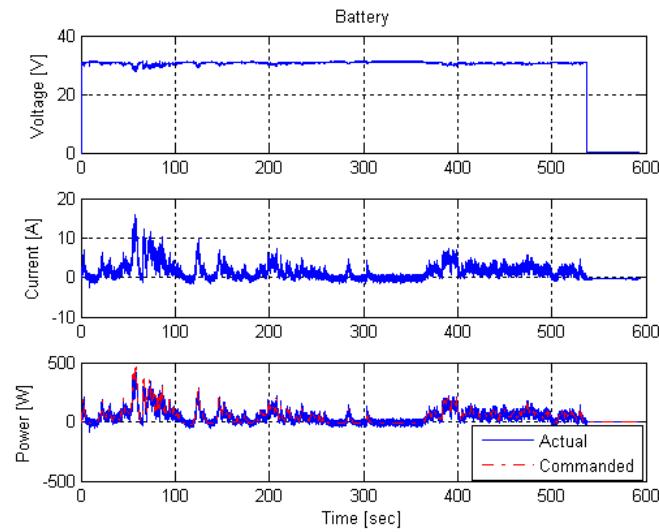


Figure 7.7: Battery testing results

The ultracapacitor results in Figure 7.8 show that the slow proportional control on the ultracapacitor is maintaining the stored energy. However, the ultracapacitor is not being utilized to its full potential, as there are still several kilojoules of energy available. This indicates that the control is still too tight and that the corner frequency of the filter is too high. If the gain,  $k_{pc}$ , is decreased or the corner frequency of the filter is lowered, the ultracapacitor will assume more of the load, relieving the battery.

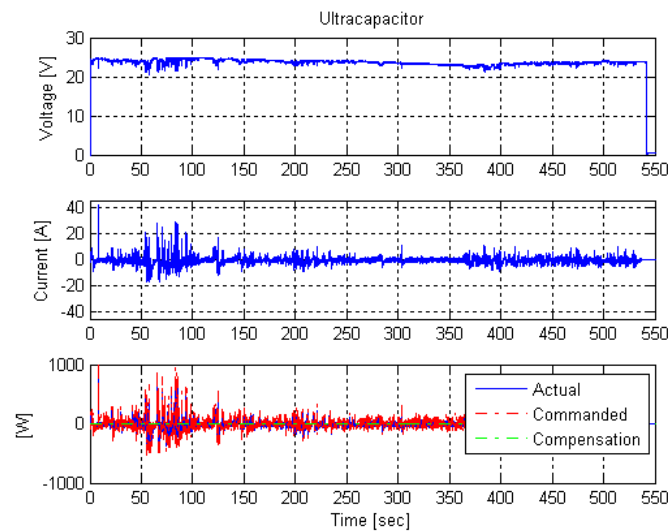


Figure 7.8: Ultracapacitor testing results

Figures 7.9-7.10 reemphasize the performance of the hybrid power architecture. The bus capacitor variables, shown in Figure 7.9, confirm that the output of the system was tightly regulated. The output voltage which was set at approximately 35 volts never varies more than one volt high or low.

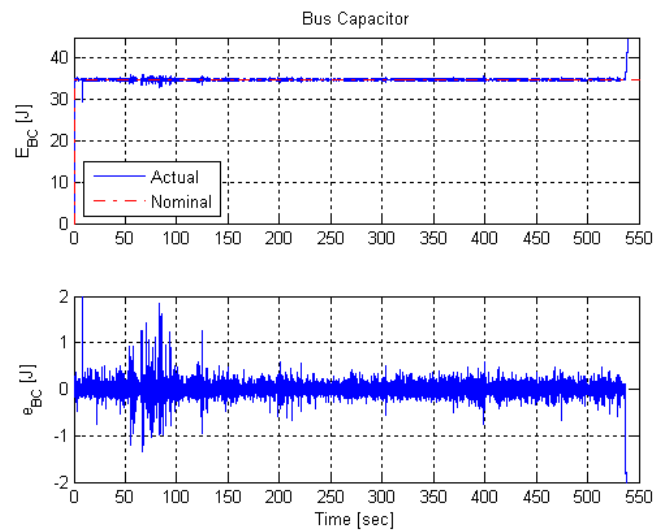


Figure 7.9: Bus capacitor testing results

Shown in Figure 7.10 is the performance of the power filtering algorithm. In the top subplot is the low frequency power, supplied by the battery, and in the bottom is shown the high frequency power which is supplied by the ultracapacitors.

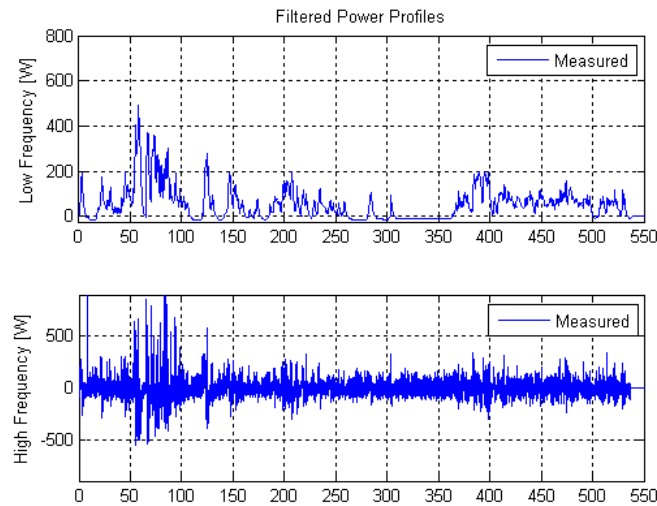


Figure 7.10: Measured high and low frequency power profiles

When compared to the complete power profile in Figure 7.4, it can be seen that the peak power supplied by the battery is reduced by nearly 300 watts, which is close to 10 amps. This indicates that the losses internal to the battery should be greatly reduced. Once again the ultracapacitor is capable of supplying more of this power, if the system gains are properly adjusted.

### Summary

The hybrid power and energy system implemented on the test bench performed very well. The dSpace hardware and software made the interaction with the system very easy. The user interface graphically showed the power split between the two devices and made the oversight of the controller possible. The supervisory controller regulated the bus capacitor energy tightly with very little error. The results of the HyPER system simulation, showing that the ultracapacitor energy decayed over the course of the tests, were verified. The gain,  $k_{pc}$ , was varied and it was shown that the control loop around the ultracapacitor could maintain the energy when the gain is properly adjusted. The filtering approach appropriately allocated the power command between

the two devices. The battery was exposed to only the low frequency components of the power demand, and the ultracapacitor was easily capable of handling the remaining energy required by the load. This chapter covered the implementation of the low-level controller proposed in chapter 3, which was able to stabilize and correctly regulate the states within the system.

## Chapter 8

### Future Work and Conclusion

#### Future Work

The HyPER system is inherently a scalable power architecture and is designed to be applied to a variety of unmanned ground vehicle platforms. However, in this thesis the system was kept small for ease of analysis and explanation. The manual setup of the low-level supervisory controller is practical as long as the energy storage devices are not going to change. It would quickly become impractical to manually configure the controller if the devices change during a mission or routine maintenance. To streamline this process, the high-level controller, mentioned at the beginning of Chapter 3, needs to become the brain of the entire power architecture. As part of the project, key components in making the architecture smart have been identified. This expanded architecture is shown in Figure 8.1.

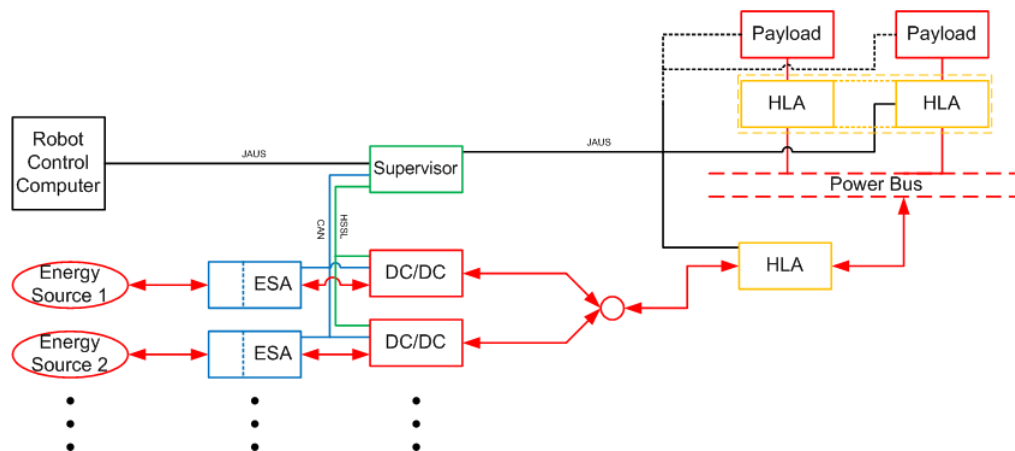


Figure 8.1: Expanded HyPER architecture

Only three of the blocks in the proposed architecture have been discussed previously. The remaining blocks enable the system's self configuration. The additional blocks are the Energy Source Adapter (ESA), the HyPER Load Adapter (HLA), and the Robot Control Computer. The Robot Control Computer is already supplied with the robot and will have some interface with the power system. The signal lines also show there are a number of different communication protocols, which will not be discussed further. In the next few paragraphs the blocks which have not been discussed in detail will be briefly explored.

### **Supervisor**

To implement the converters in a power delivery system there must be a supervisor coordinating the energy devices. The supervisory controller should be implemented in a digital processing environment as a two-level controller for the hybrid architecture to be viable. A low-level controller is required that is capable of maintaining the main robot power bus by generating current commands for each converter in the system, as has been previously discussed, as well as a high-level controller to manage the storage devices and low-level controller.

The high-level portion of the supervisor has three main functions. First, it configures the low-level controller any time the operating conditions change. The supervisor communicates with the main robot controller via the JAUS protocol, an open architecture developed specifically for unmanned systems, to enable the operator to change the operating conditions, i.e. change the energy sources in use. Second, it monitors the devices through a CAN communication link to the ESAs. This includes ensuring all energy storage devices are within safety limits, calculating state of charge, and recording real time current and voltage. Lastly, the controller must also be able to control devices based on the overall system's state of charge, or based on a particular mission's requirements. For example it must be capable of activating a generator or placing a battery in

charge mode. Beyond these main functions, there are many other potential applications for the high-level controller. These could include health monitoring algorithms, energy optimization, mission energy requirement estimation, mission programmable operation modes, and primary and auxiliary load control.

### **Energy Source Adapter**

The Energy Source Adapter's function is to facilitate the integration of any energy storage device into the HyPER system. Physically, the ESA converts the connector on the storage device to a connector compatible with the converter. Logically, it provides much more to the system. It communicates through a CAN link to the supervisor in order to send it data about the energy storage device. This data includes operating data such as current, voltage, and state of charge, and also includes the operating characteristics of the device. These operating parameters allow the supervisory controller to automatically discover and manage the device. This auto discovery function is key to enabling the HyPER system's self-configuration. The operating parameters of the device inform the supervisory controller how to configure the low-level controller in order to optimally utilize the energy available. The final function of the ESA is to provide the supervisory controller with the capability to control the operating mode of the device, such as allowing the supervisory controller to place a BB2590 in charge mode.

### **HyPER Load Adapter**

The HyPER Load Adapter provides control over a robot's payload and uses the JAUS protocol to communicate with the supervisory controller. The HLA provides the supervisor with the operating parameters of the payload, monitors the power usage and health of the payload, and

provides the capability to completely shut down the payload. The adapter could be implemented as a standalone device or as an integrated part of the robotic platform.

## **Conclusion**

As the use of robots spreads to different applications, their power and energy systems must be able to adapt to the wide variety of operating conditions which could be encountered. The scalable hybrid power and energy architecture proposed in this thesis can be used on these robots to allow adaptation to the operating conditions.

A simple scalable bidirectional converter was developed as the core of the architecture, and the design and operation was discussed. Later, the efficiency of the converter was found by testing a single converter at different operating set points. It was found that the converter efficiency was over 95% for all but the lowest power transfers.

The design of the supervisory controller was initiated with a short discussion on what it must accomplish, but the scope of the thesis dictated that only the low-level controller be discussed. The low-level controller was developed and a HyPER system model was developed. It was shown how this feedback system could be expanded to accommodate multiple energy storage devices.

Before implementing the HyPER system in hardware, the system was simulated to show that the approach taken to designing the hardware and the supervisory controller was a viable approach. The modeling of each system component was discussed and the results of the simulation were shown. The results indicated the system would function properly, however, it was noted that the energy stored in the ultracapacitor decayed over time. A compensation controller was added to ensure that the ultracapacitor was able to continuously function. The

results from the simulation with this modification indicated the system would function properly in extended continuous operation.

In any controlled system it should be shown that the system is stable during operation. The simulation of the system did not show that it would become unstable during operation; however, that is not sufficient proof of stability. The system was simplified in such a way that allowed the use of linear control theory to analyze the stability of a mathematical model of the system. This model used the energy of the ultracapacitor and the bus capacitor as its primary states. It was shown that the eigenvalues of the system lie in the left half of the complex plane over a range of controller set points. This is sufficient to show that the system is stable under the normal operating conditions. It was also shown that this analysis is sufficient to show the system is stable even when multiple other energy storage devices are in the system.

Finally, a test bench of the system was built and instrumented. A real world robotic power profile was applied to the system, and the HyPER system was able to stabilize the energy in the bus capacitor for the duration of the load. The ultracapacitor also maintained its energy under continuous operation. The results of this testing conclusively showed that the HyPER system as proposed could be used as a scalable hybrid power and energy system for unmanned ground vehicles.

## Bibliography

1. Horowitz, Paul, and Winfield Hill. The Art of Electronics. 2<sup>nd</sup> ed. Cambridge: Cambridge University Press, 1995
2. Mohan, Ned, Tore M. Undeland, and William P. Robbins. Power Electronics: Converters, Applications, and Design. 3<sup>rd</sup> ed. Hoboken: John Wiley & Sons, INC., 2003
3. “Powder Cores.” Magnetics. 2008. Magnetics, February 2009 <[http://www.mag-inc.com/File%20Library/Product%20Literature/Powder%20Core%20Literature/2008\\_PowderCoreCatalog.pdf](http://www.mag-inc.com/File%20Library/Product%20Literature/Powder%20Core%20Literature/2008_PowderCoreCatalog.pdf)>
4. “Inductor Design in Switching Regulators.” Magnetics. 2008, Magnetics, February 2009 <<http://www.mag-inc.com/File%20Library/Product%20Literature/General%20Information/ps-02.pdf>>
5. “CO55867A2.” Magnetics. 2009, Magnetics, February 2009 <http://www.mag-inc.com/File%20Library/Product%20Datasheets/Powder%20Core/New%20Powder%20Cores/Toroids/866%20Size/C055867A2.pdf>
6. Garcia, F. S., A. A. Ferreira, and J. A. Pomilio “Control Strategy for Battery-Ultracapacitor Hybrid Energy Storage System.” Twenty-Fourth Annual IEEE Applied Power Electronics Conference and Exposition, 2009. 15-19 Feb. 2009: 826 - 832

7. Ghaderi, A., A. Sanada, A.A.F. Nassiraei, K. Ishii, and I. Godler. "Power and propulsion systems design for an autonomous omni-directional mobile robot." Twenty-Third Annual IEEE Applied Power Electronics Conference and Exposition, 2008. 24-28 Feb. 2008: 267 – 272
8. Ogawa, Kazuya, Hyonju Kim, Makoto Mizukawa, and Yoshinobu Ando. "Development of the Robot Power Management System Adapting to Tasks and Environments -The design guideline of the Power Control System Applied to the Distributed Control Robot." SICE-ICASE, 2006. 18-21 Oct. 2006: 2042 - 2046
9. Ortuzar, M., J. Dixon, and J. Moreno. "Design, construction and performance of a buck-boost converter for an ultracapacitor-based auxiliary energy system for electric vehicles." The 29th Annual Conference of the IEEE Industrial Electronics Society, 2003. 2-6 Nov. 2003: 2889 - 2894 Vol.3
10. Riofrio, J.A., and E. J. Barth. "Design of a Free Piston Pneumatic Compressor as a Mobile Robot Power Supply." Proceedings of the 2005 IEEE International Conference on Robotics and Automation, 2005. 18-22 April 2005: 235 - 240
11. Shu-mei, Cui, Tian De-wen, and Zhang Qian-fan. "Study of hybrid energy control strategy for hybrid electric drive system in All Electric Combat Vehicles." IEEE Vehicle Power and Propulsion Conference, 2008. 3-5 Sept. 2008: 1 – 5

12. Wang, Tiecheng, Haifang Yu, and Chunbo Zhu. “Hybrid energy sources for hybrid electric vehicle propulsion.” IEEE Vehicle Power and Propulsion Conference, 2008. 3-5 Sept. 2008: 1 – 4
  
13. Zhang, Yu, Zhenhua Jiang, and Xunwei Yu. “Control Strategies for Battery/Supercapacitor Hybrid Energy Storage Systems”. IEEE Energy 2030 Conference, 2008. 17-18 Nov. 2008:1 – 6
  
14. iRobot®. “iRobot® PackBot®.” January 31, 2010 < <http://www.sugv300series.com/>>
  
15. Foster-Miller. “TALON Family of Military, Tactical, EOD, MAARS, CBRNE, Hazmat, Swat, and Dragon Runner Robots.” January 31, 2010. < <http://www.foster-miller.com/lemming.htm>>
  
16. Lockheed Martin. “Multifunction Utility/Logistics and Equipment Vehicle (MULE).” January 31, 2010. < <http://www.lockheedmartin.com/products/mule/index.html>>

## Appendix A.

### Inductor Design Parameters

The design of the inductor itself was accomplished by following the manufactures design procedures, and is shown below. The manufacturer's design specifications and procedures can be found in [3-5].

$L_{desired}$	$I_{max}$	$\mu_{core}$	$A_{L,nom}$
$30\mu H$	$40 A$	$60$	$68 \text{ }^nH / \text{Turn}^2$

Table A.1: Inductor specifications

Derate the nominal inductance of the core by 8% as specified by the manufacturer.

$$A_{L,min} = 0.92 A_L = 62.56 \text{ }^nH / \text{Turn}^2 \quad \text{A.1}$$

Calculate the number of turns needed.

$$N = \sqrt{\frac{L}{A_{L,min}}} \text{ Turns} = 21.898 \text{ Turns} \quad \text{A.2}$$

Calculate the bias.

$$H = \frac{N \times I}{l} \frac{A \cdot \text{Turns}}{cm} = 43.633 \frac{A \cdot \text{Turns}}{cm} \quad \text{A.3}$$

From a manufacturer table determine the roll off of the initial permeability for the bias calculated previously. The number of turns is derated by the provided duration constant,  $\mu_{pu} = 0.7$ , to obtain the desired inductance.

$$N = \frac{N}{\mu_{pu}} = 31.28 \text{ Turns} \quad \text{A.4}$$

This is the number was rounded to 30 turns as the inductor will not be normally be operating at full capacity. Thus the nominal inductance is given in equation A.5.

$$L = 68 \times 30^2 = 54\mu H \quad \text{A.5}$$

This inductor is significantly larger than the 30  $\mu H$  needed, but this helps to minimize the output current ripple. The downside is that the conduction losses will be significantly higher. A lower inductance would result in fewer turns which would in turn reduce the winding resistance. The inductor design is now complete. Before construction, the losses resulting from the core loss and the conduction losses can be estimated. First consider the core losses. An rms current of  $I_{rms} = 2.88 \text{ A}$ , translates into a magnetizing force and flux density shown by the equations below.

$$f_m = 0.795 \cdot H = 3.5903 \text{ Orstedes} \quad \text{A.6}$$

$$B = \left[ \frac{0.2576 + (5.9 \times 10^{-2})f_m + (1.208 \times 10^{-4})f_m^2}{1 + (1.97 \times 10^{-2})f_m + (4.78 \times 10^{-4})f_m^2} \right]^2 = 0.1933 \text{ kgauss} \quad \text{A.7}$$

According to the manufacture's specifications, the core loss can then be calculated by the following equations where V is the volume of the core.

$$P_L = 0.625B^{2.24}f_s^{1.41} = 10.396 \text{ mW/cm}^3 \quad \text{A.8}$$

$$P_{core} = V \cdot P_L = 0.3607 \text{ W} \quad \text{A.9}$$

This seems like a negligible loss when the power being converted is on the order of a kilowatt, but the conduction losses of the inductor still need to be calculated. It can be shown through the manufacture's specifications and parameters of the inductor that the estimated resistance of the windings is  $R_{winding} = 5.4 \text{ m}\Omega$ . The conduction losses of the inductor can then be described by equation A.10.

$$P_{Conduction} = I^2 R_{winding} \quad \text{A.10}$$

Figure 2.4 shows the estimated inductor losses, which are based on the design and loss mechanism calculations outlined in this appendix.

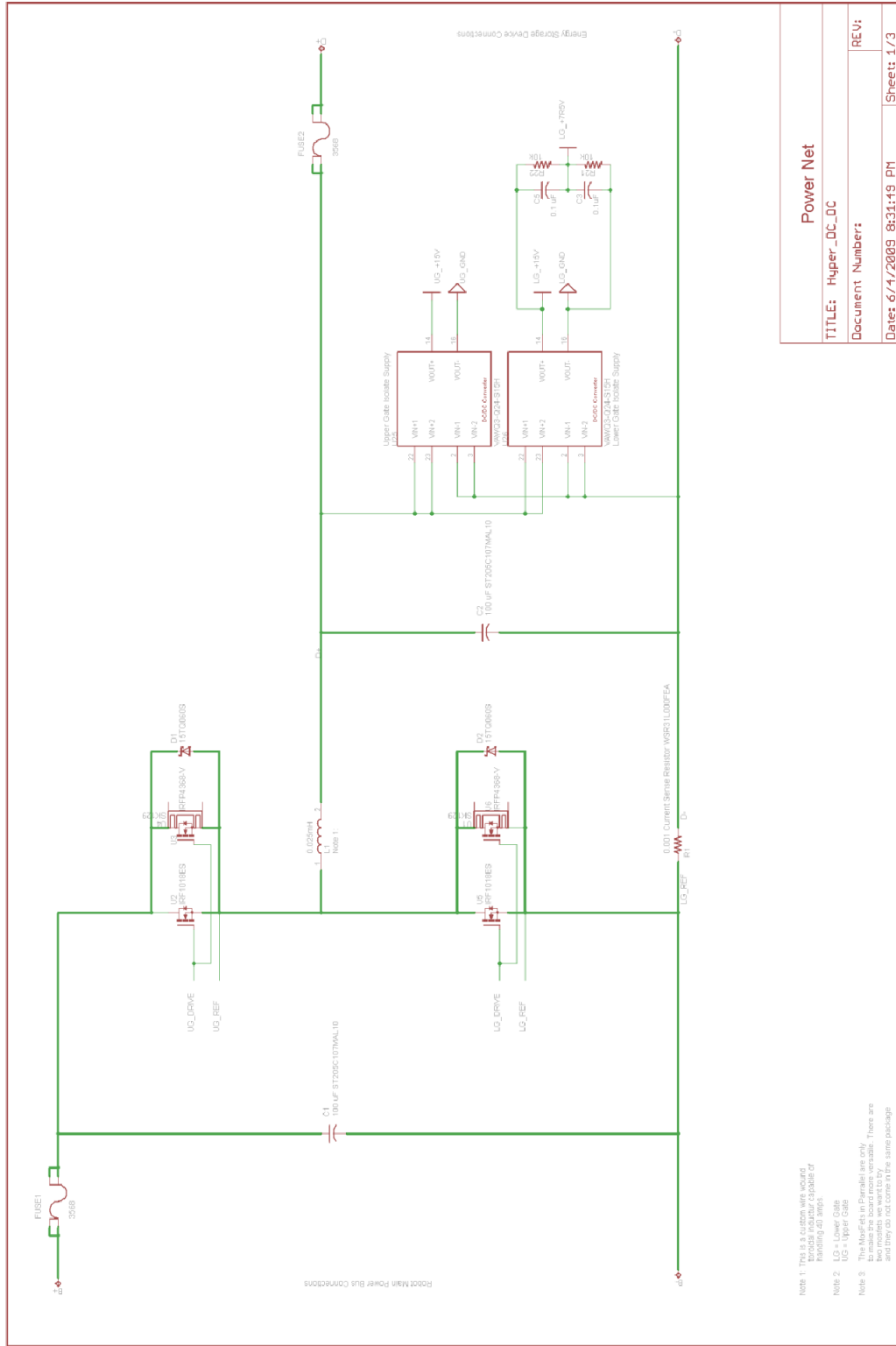
## **Appendix B.**

### **Bidirectional Converter Schematics, Parts List, and PCB Layout**

The following three pages contain the schematics for the HyPER system bidirectional DC-DC converter. It should be noted that in the 'Power Net' schematic there are two sets of MOSFETs shown. In the actual circuit there is only one set. It was only shown this way in the schematic because two sets of MOSFETs with different packages were considered for the initial design.

It should also be noted that the values for the resistors in the schematics may not be what was actually installed on the board. A number of values were changed during testing of the circuit, in order to optimize its efficiency and performance. The final values are reflected in Tables B.1 and B.2.

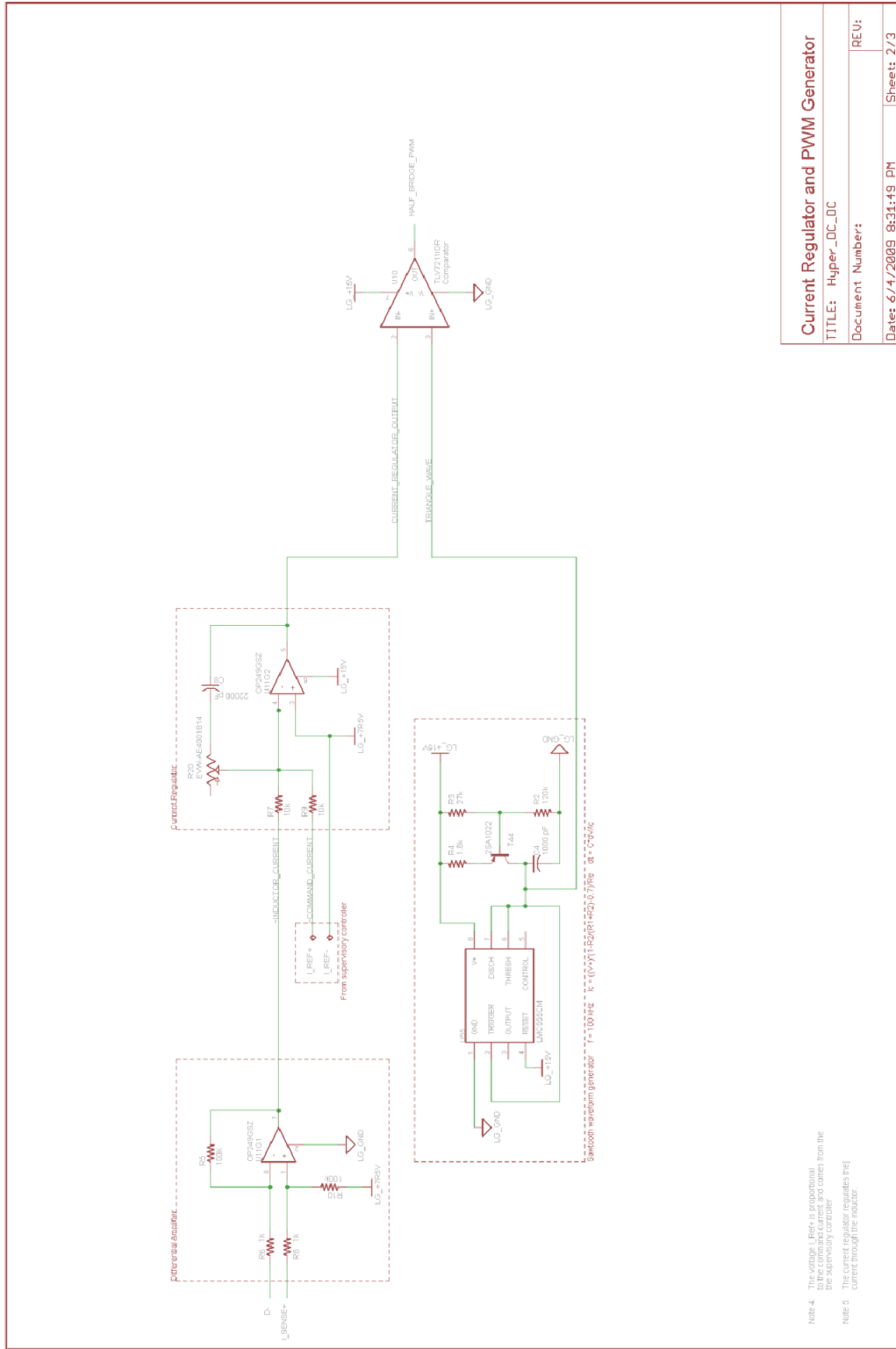
Finally, Figures B.4-B.5 show the printed circuit board layout. The PCB is a four layer board, but only the top and bottom layers are shown. The outer layers are 4oz copper layers on account of the large amounts of current they must be able to conduct for extended periods of time.



Note 1: This is a current sensitive circuit. Excessive inrush current may damage the components.  
 Note 2: LG - Lower Gate  
 Note 3: The IGBTs in Parallel are only used for high current applications. There are two models, we want to try and they do not come in the same package.

<b>Power Net</b>	
TITLE: Hyper_DC_DC	
Document Number:	REV:
Date: 6/1/2009 8:31:19 PM	Sheet: 1 / 3

Figure B.1 Converter power net schematic



<b>Current Regulator and PWM Generator</b>	
TITLE: Hyper_DC_DC	
Document Number:	REV:
Date: 6/4/2009 8:31:49 PM	Sheet: 2/3

Figure B.2: Converter control circuitry schematic

NOTE 4: The voltage I\_Pref+ is proportional to the converter current and comes from the supervisory controller.  
 NOTE 5: The supervisory controller supplies the current through the inductor.



Designator	Value	Description
C1	100 $\mu$ F	Input Capacitor
C2	100 $\mu$ F	Output Capacitor
C3	2.2 $\mu$ F	805 Capacitor
C4	1000pF	805 Capacitor
C5	2.2 $\mu$ F	805 Capacitor
C8	22000pF	805 Capacitor
C9	10nF	805 Capacitor
C10	10nF	805 Capacitor
C11	10nF	805 Capacitor
C12	10nF	805 Capacitor
L1	0.035mH	Toroidal Inductor
R1	0.001 $\Omega$	Power Metal Strip Resistor
R2	120k $\Omega$	805 Resistor
R3	27k $\Omega$	805 Resistor
R4	1.8k $\Omega$	805 Resistor
R5	100k $\Omega$	805 Resistor
R6	10k $\Omega$	805 Resistor
R7	4.7k $\Omega$	805 Resistor
R8	10k $\Omega$	805 Resistor
R9	4.7k $\Omega$	805 Resistor
R10	100k $\Omega$	805 Resistor
R11	3k $\Omega$	805 Resistor
R12	5.1k $\Omega$	805 Resistor
R14	2 $\Omega$	805 Resistor
R15	0	805 Resistor
R16	5k $\Omega$	805 Resistor
R17	5k $\Omega$	805 Resistor
R18	6.8k $\Omega$	805 Resistor
R19	2 $\Omega$	805 Resistor
R20	10k $\Omega$ $\pm$ 30%	Potentiometer
R21	1k $\Omega$	805 Resistor
R22	1k $\Omega$	0805 Resistor
R24	6.8k $\Omega$	0805 Resistor

Table B.1: Converter passive device definitions

Designator	Part Number	Description
D1	VS-15TQ060S	Schottky Diode
D2	VS-15TQ060S	Schottky Diode
D3	PMEG2010AEH	Schottky Diode
D4	DFLZ5V17	Zener Diode
D5	PMEG2010AEH	Schottky Diode
D6	DFLZ5V17	Zener Diode
FUSE1	3568	Fuse Holder
FUSE2	3568	Fuse Holder
T44	2SA10220CL	PNP Bipolar Transistor
U1	SK129	Heat Sink
U2	IRF1018ES	N-Channel MosFet
U3	IRFP4368PBF	N-Channel MosFet
U4	SK129	Heat Sink
U5	IRF1018ES	N-Channel MosFet
U6	IRFP4368PBF	N-Channel MosFet
U10	TLV7211IDR	Comparator
U11	OP249GSZ	Opamp
U12	HCPL-0201-500E	Optocoupler
U13	MIC4422YM TR	Gate Drive
U14	IRS21091STRPBF	Half Bridge Gate Drive
U15	HCPL-0201-500E	Optocoupler
U16	MIC4422YM TR	Gate Drive
U25	VAWQ3-Q24-S15H	Isolated DC Supply
U26	VAWQ3-Q24-S15H	Isolated DC Supply
U55	LMC555CM	CMOS 555 Timer

Table B.2: Converter active device definitions

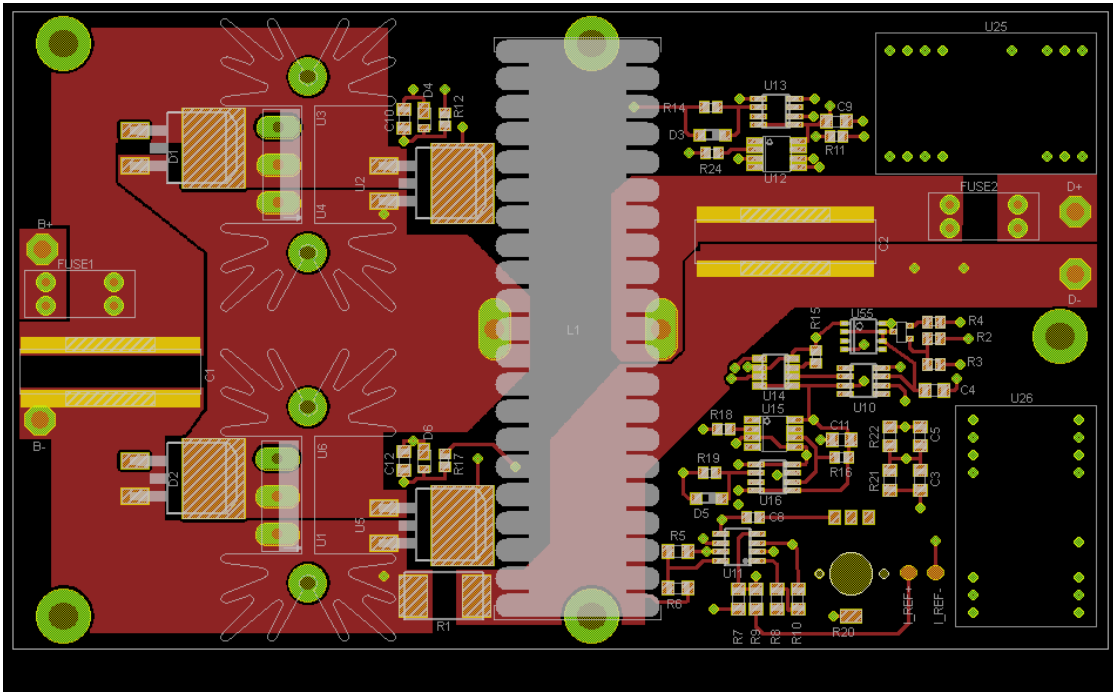


Figure B.4: PCB layout top layer

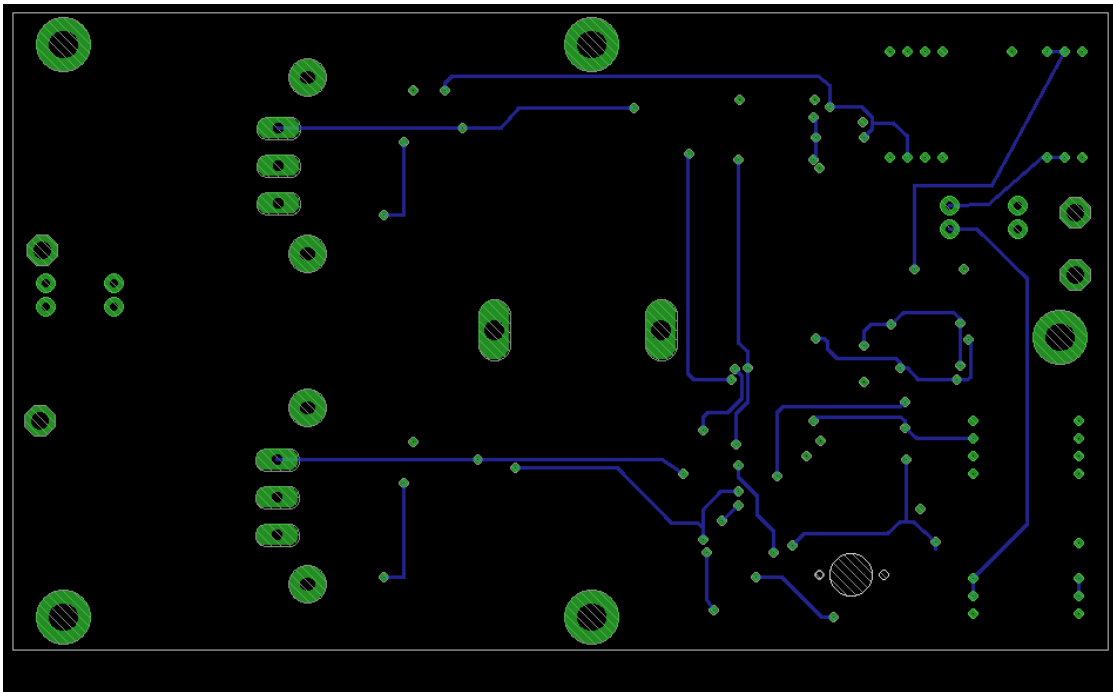


Figure B.5: PCB layout bottom layer

## Appendix C.

### SIMULINK® Simulations

The following simulation is control system simulation diagram. Figure C.1 shows the main diagram.

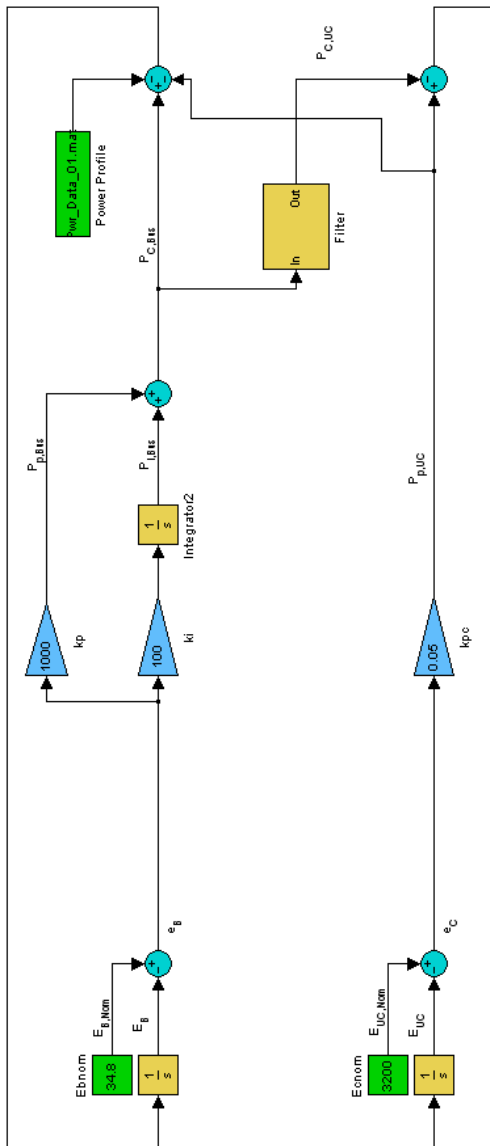


Figure C.1: Control system simulation main system

The only subsystem present in the control simulation is the filter, shown in Figure C.2.

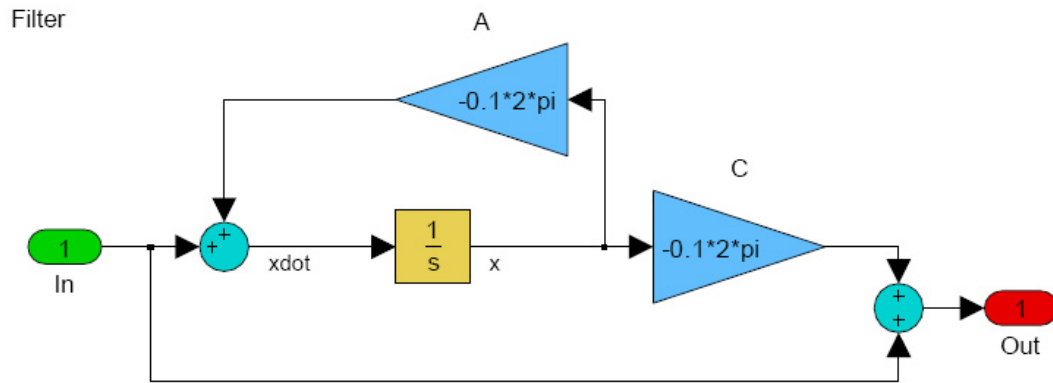


Figure C.2: Filter algorithm subsystem

The next set of figures show the SIMULINK® diagrams for the full HyPER system simulation. It has many different subsystems which include capacitor models, a filtering model, main controller model, a capacitor charging circuit, and a lumped battery/generator model. As discussed in Chapter 4, the lumped battery/generator model contains not only the storage device models, but also their respective converter models.

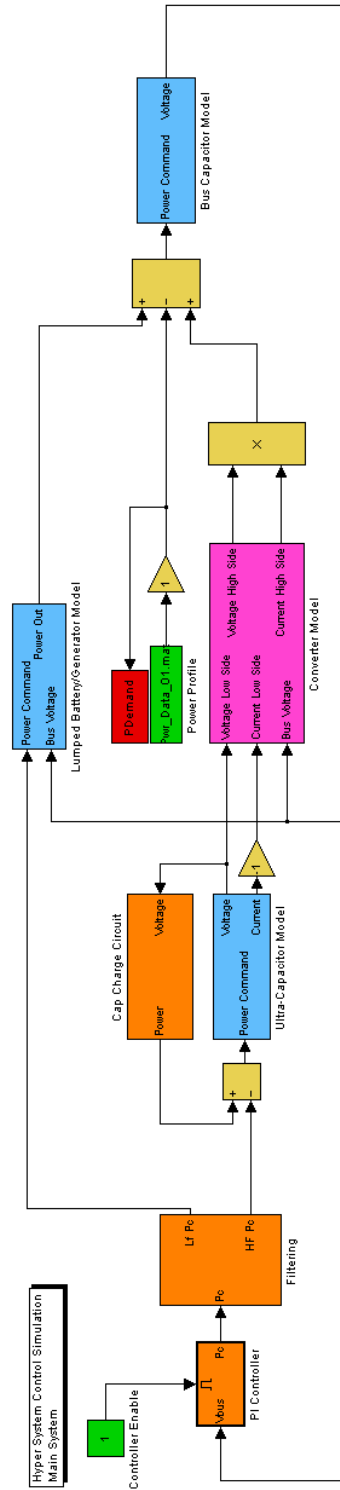


Figure C.3: HyPER system simulation main

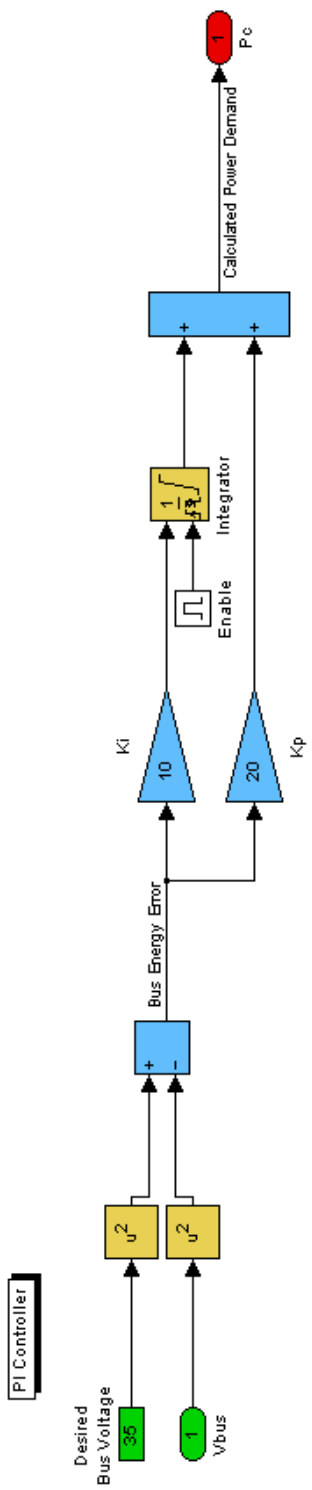


Figure C.4: PI controller subsystem

### Capacitor Charging Circuit

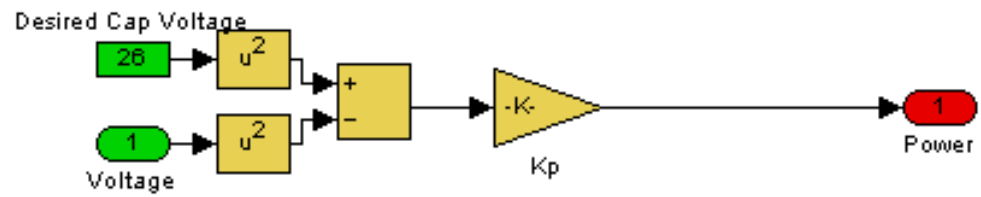


Figure C.5: Capacitor charge circuit subsystem

### Filter

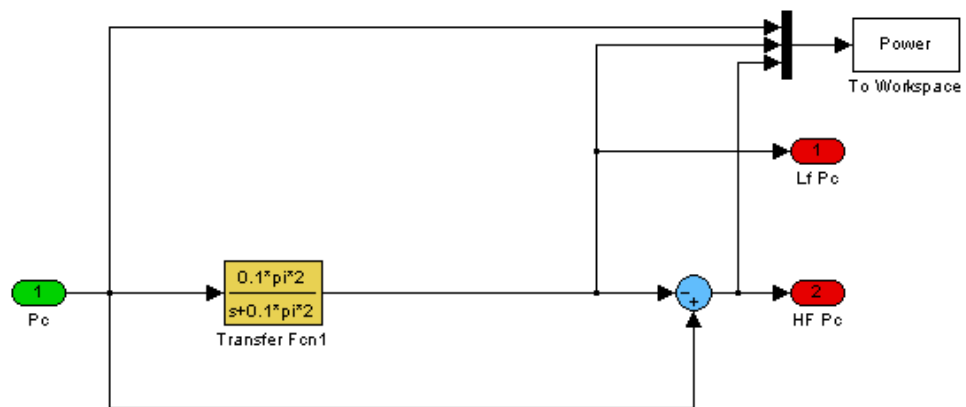


Figure C.6: Filter algorithm subsystem

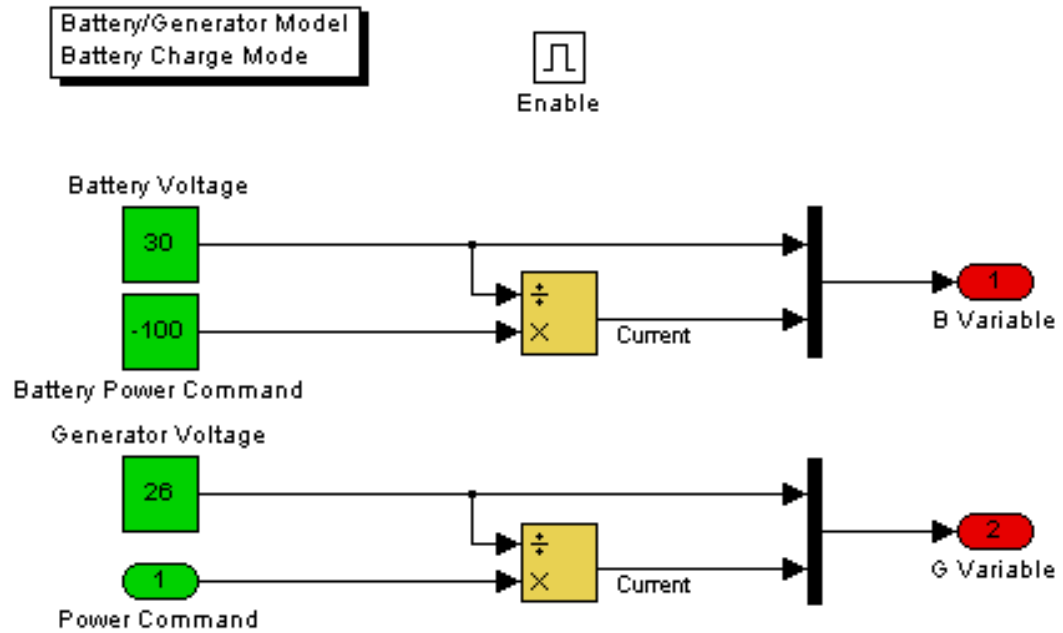


Figure C.7: Lumped batter/generator model (battery charge mode)

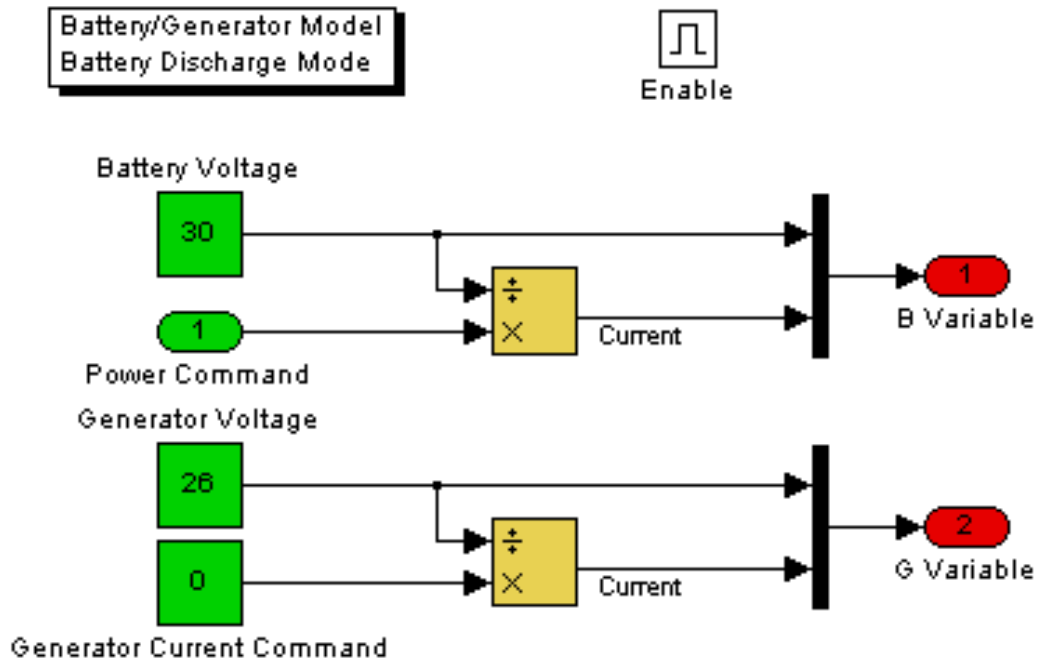


Figure C.8: Lumped battery/generator model (battery discharge mode)

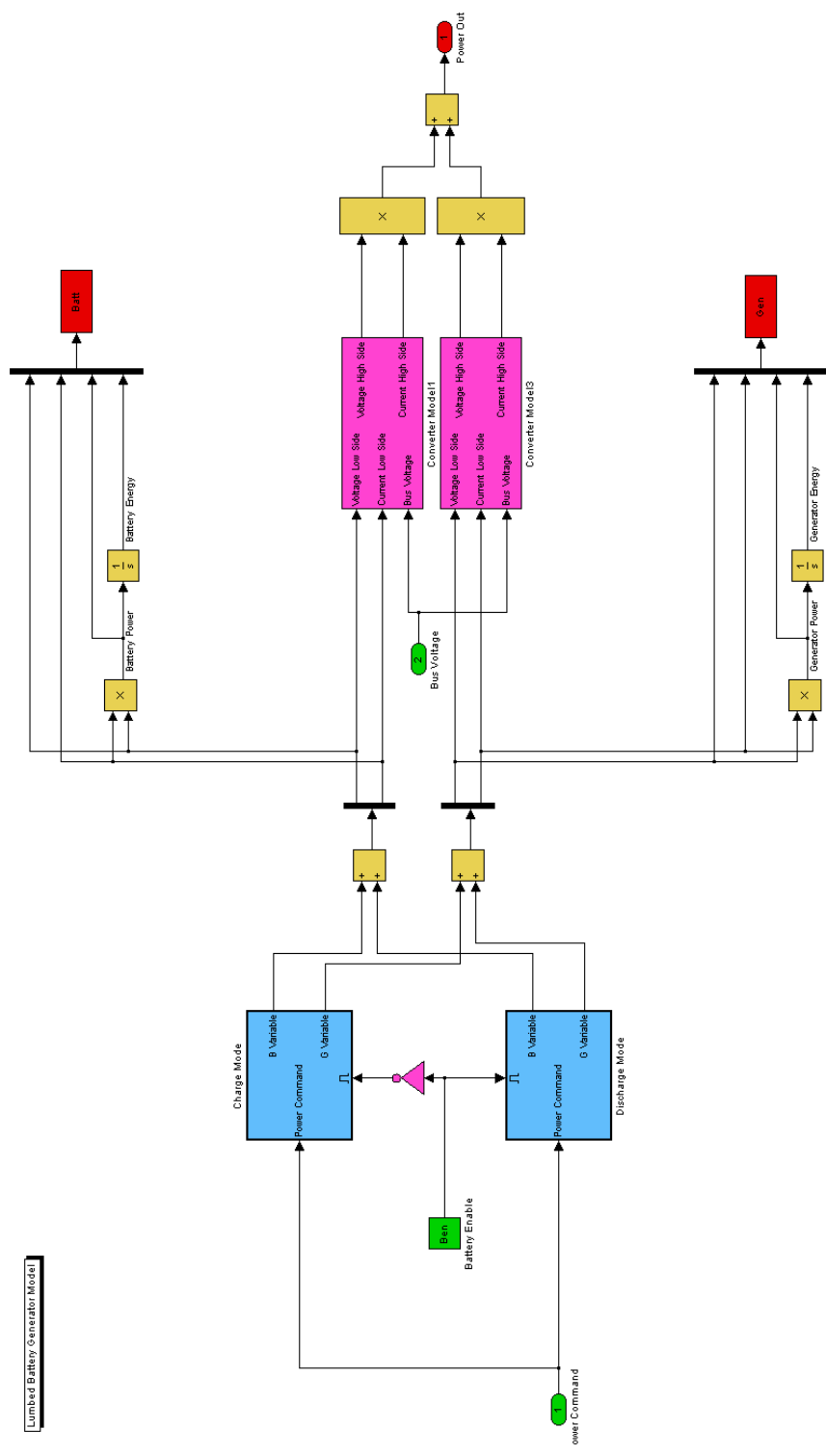


Figure C.9: Low frequency source subsystem

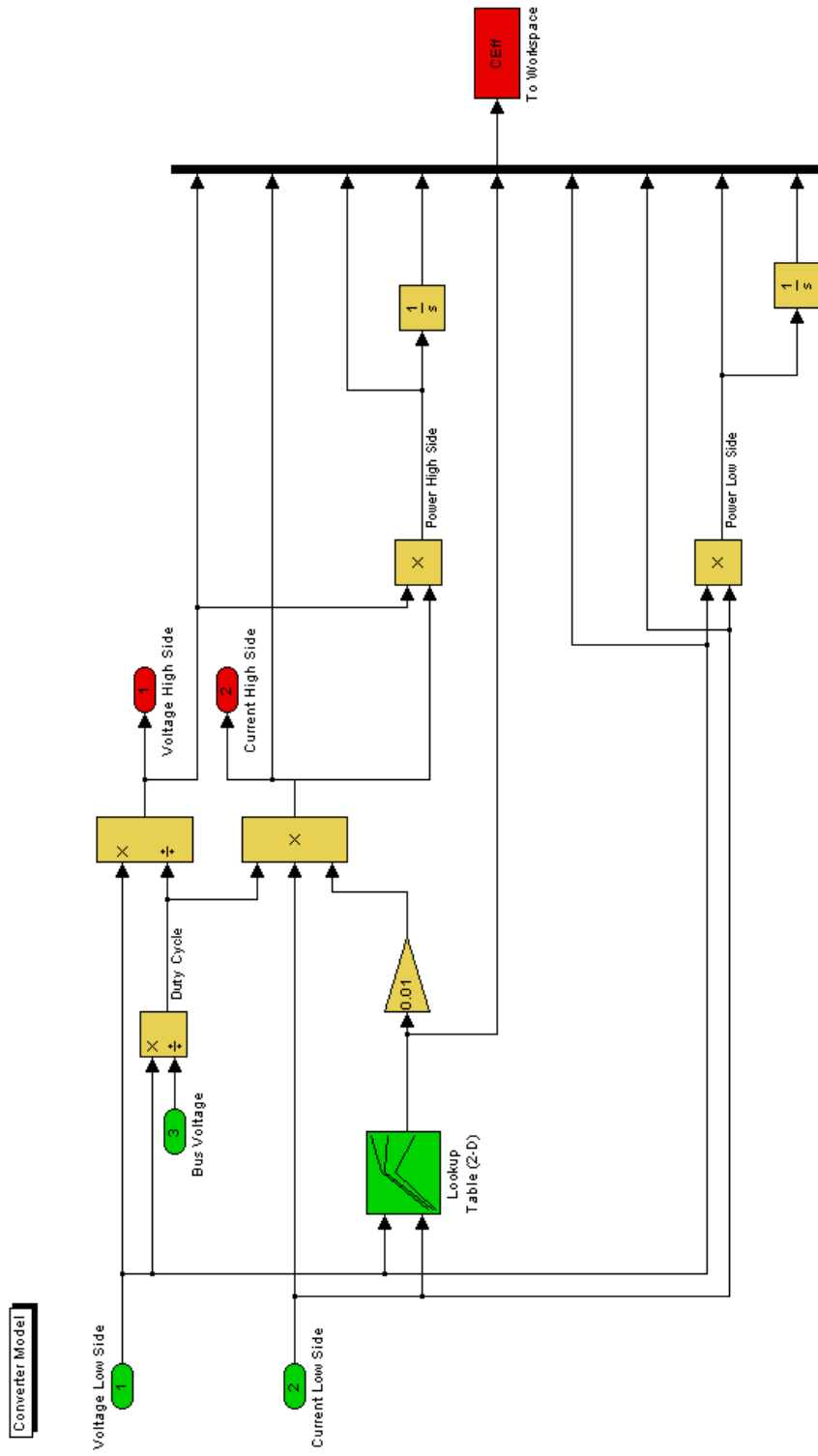


Figure C.10: Converter model subsystem



## Appendix D.

### dSpace Controller and Interface

This appendix shows the supervisory controller implemented in SIMULINK®. This SIMULINK® code is then compiled into C and implemented on the dSpace DS1104 real time controller board. Any signal in the SIMULINK® diagram can be accessed from the dSpace user interface, Control Desk. Control Desk can be configured by the user to display any information needed, and can also be used to manipulate the controller, i.e. change set points, start, stop, etc. The specific interface used in the implementation of the HyPER system used for this thesis is shown in Figure D.7.

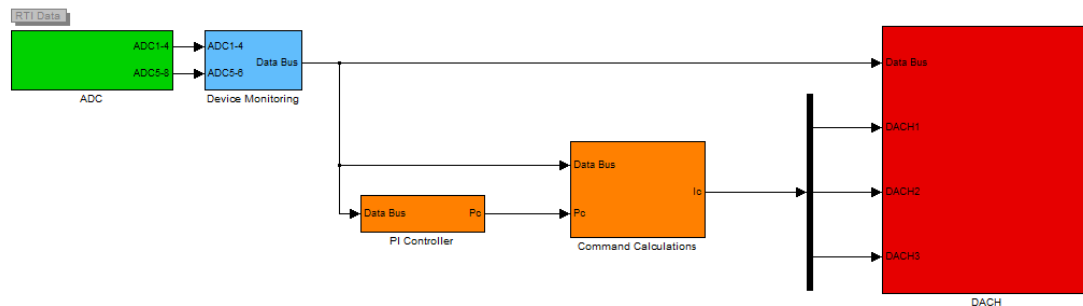


Figure D.1: dSpace SIMULINK® controller

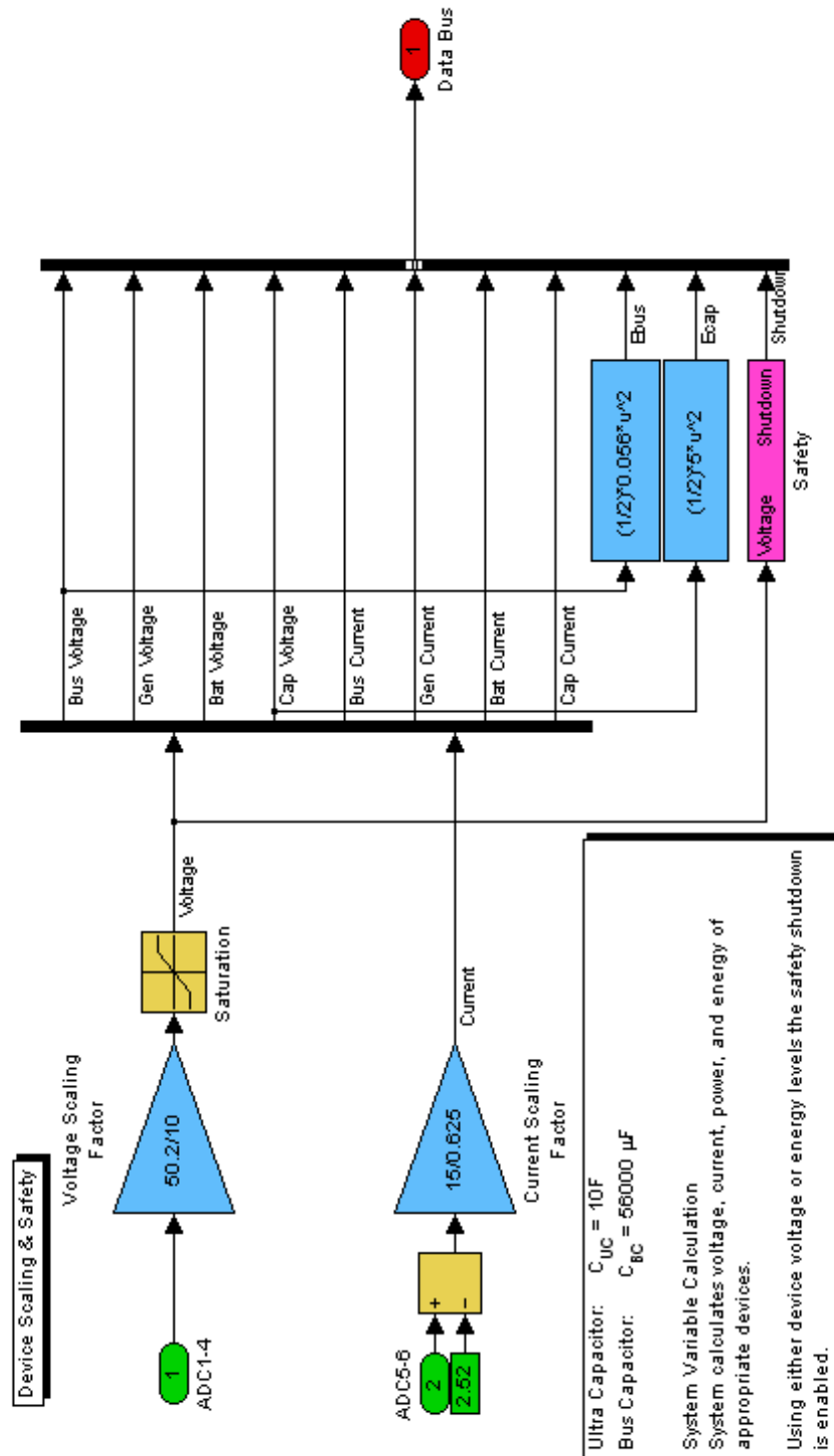


Figure D.2: Device DAQ and monitoring

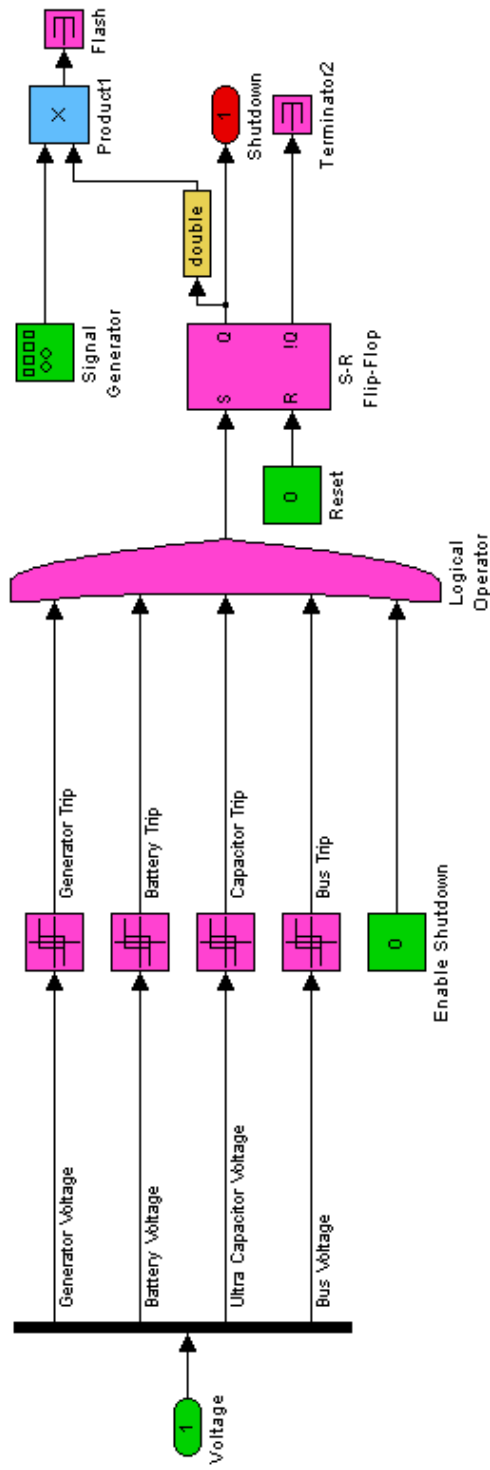


Figure D.3: Safety override subsystem

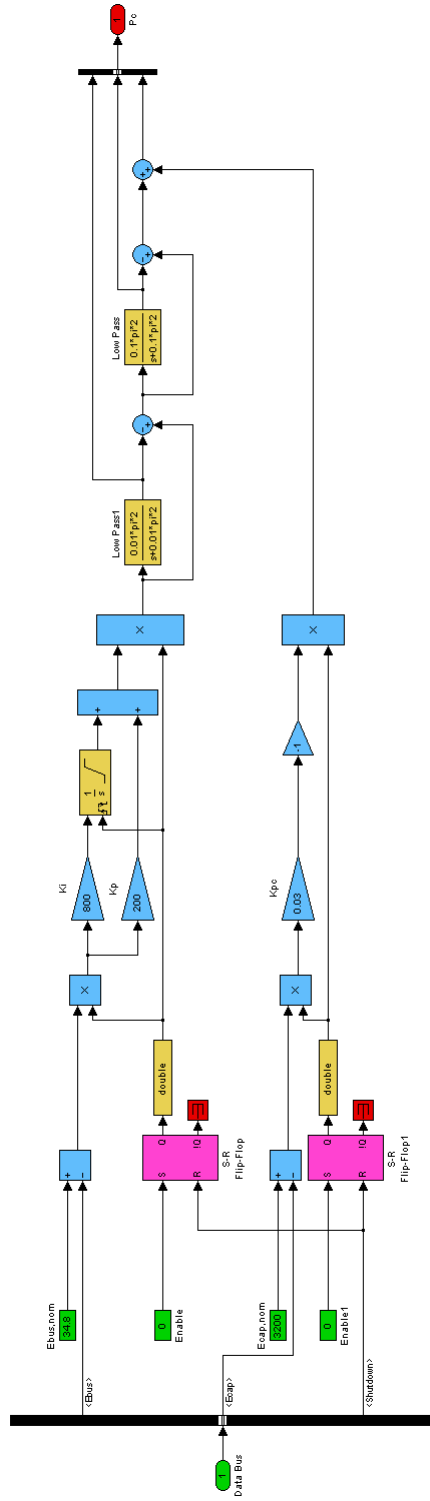


Figure D.4: Controller subsystem

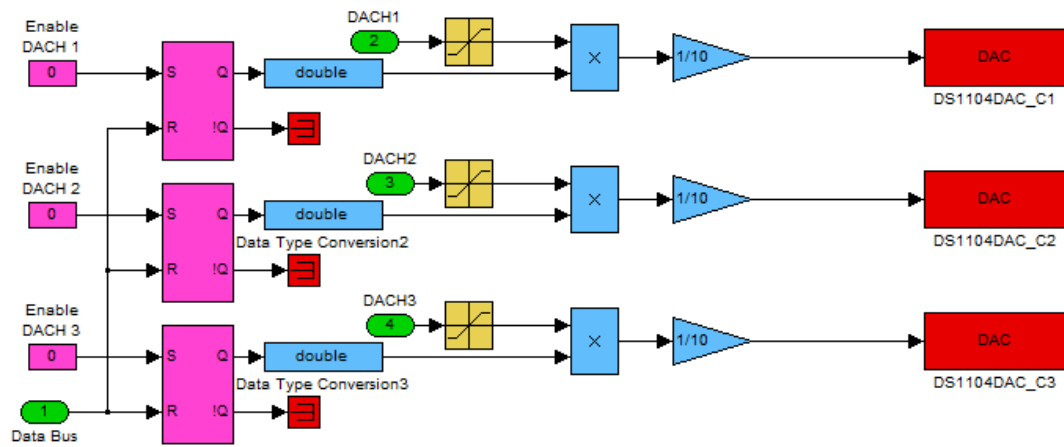


Figure D.5: dSpace D/A interface subsystem

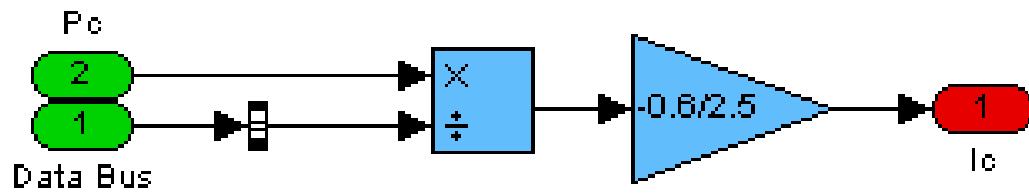


Figure D.6: Current command calculation subsystem

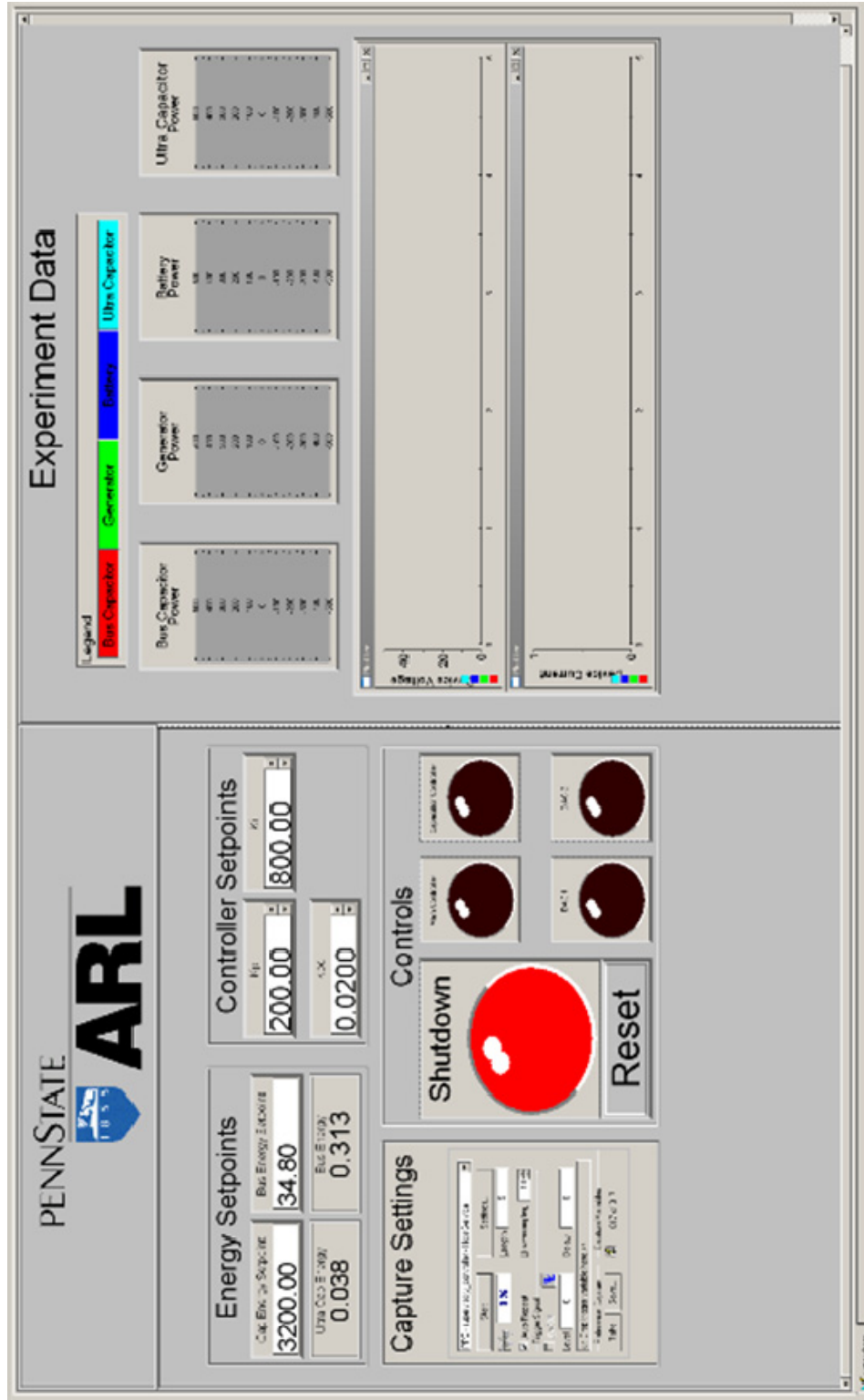


Figure D.7: dSpace Control